Coupled wind-forced controls of the Bering–Chukchi shelf circulation and the Bering Strait throughflow: Ekman transport, continental shelf waves, and variations of the Pacific–Arctic sea surface height gradient

CrossMark

Seth L. Danielson [a,*], Thomas J. Weingartner [a], Katherine S. Hedstrom [b], Knut Aagaard [c], Rebecca Woodgate [c], Enrique Curchitser [d], Phyllis J. Stabeno [e]

[a] School of Fisheries and Ocean Science, Institute of Marine Science, University of Alaska Fairbanks, Fairbanks, AK 99775-7220, USA
[b] Arctic Region Supercomputing Center, University of Alaska Fairbanks, Fairbanks, AK 99775, USA
[c] Polar Science Center, Applied Physics Laboratory, University of Washington, Seattle, WA, USA
[d] Institute of Marine and Coastal Sciences, Rutgers University, New Brunswick, NJ 08901, USA
[e] Pacific Marine Environmental Laboratory, NOAA, 7600 Sand Point Way, Seattle, WA 98115-6349, USA

ARTICLE INFO

ABSTRACT

We develop a conceptual model of the closely co-dependent Bering shelf, Bering Strait, and Chukchi shelf circulation fields by evaluating the effects of wind stress over the North Pacific and western Arctic using atmospheric reanalyses, current meter observations, satellite-based sea surface height (SSH) measurements, hydrographic profiles, and numerical model integrations. This conceptual model suggests Bering Strait transport anomalies are primarily set by the longitudinal location of the Aleutian Low, which drives oppositely signed anomalies at synoptic and annual time scales. Synoptic time scale variations in shelf currents result from local wind forcing and remotely generated continental shelf waves, whereas annual variations are driven by basin scale adjustments to wind stress that alter the magnitude of the along-strait (meridional) pressure gradient. In particular, we show that storms centered over the Bering Sea excite continental shelf waves on the eastern Bering shelf that carry northward velocity anomalies northward through Bering Strait and along the Chukchi coast. The integrated effect of these storms tends to decrease the northward Bering Strait transport at annual to decadal time scales by imposing cyclonic wind stress curl over the Aleutian Basin and the Western Subarctic Gyre. Ekman suction then increases the water column density through isopycnal uplift, thereby decreasing the dynamic height, sea surface height, and along-strait pressure gradient. Storms displaced eastward over the Gulf of Alaska generate an opposite set of Bering shelf and Aleutian Basin responses. While Ekman pumping controls Canada Basin dynamic heights (Proshutinsky et al., 2002), we do not find evidence for a strong relation between Beaufort Gyre sea surface height variations and the annually averaged Bering Strait throughflow. Over the western Chukchi and East Siberian seas easterly winds promote coastal divergence, which also increases the along-strait pressure head, as well as generates shelf waves that impinge upon Bering Strait from the northwest.

1. Introduction

1.1. Background

This study is motivated by the need to reconcile the following observations of the Bering/Chukchi circulation field (Fig. 1). Current meter records show that the annual mean northward Bering Strait transport increased from 2001 to 2011 (Woodgate et al., 2012). From 2006–2011, the mean winter position of the Aleutian Low shifted eastward into the Gulf of Alaska (Danielson et al., 2011a; Overland et al., 2012) relative to a more westward position over the Bering Sea from 2000–2005. In contrast, Danielson et al. (2012a,b) show that an eastward-displaced Aleutian Low results in more northerly winds over the central Bering shelf that force anomalously southward advection there, suggesting that transport in Bering Strait should have decreased in the latter half of the decade, rather than increased. We here construct an integrated view of the Bering/Chukchi shelf circulation field that is consistent with these observations by determining (1) the effect of remote wind forcing over the Bering and Chukchi shelves and their adjacent basins on the flow through the Bering Strait; and (2) the time
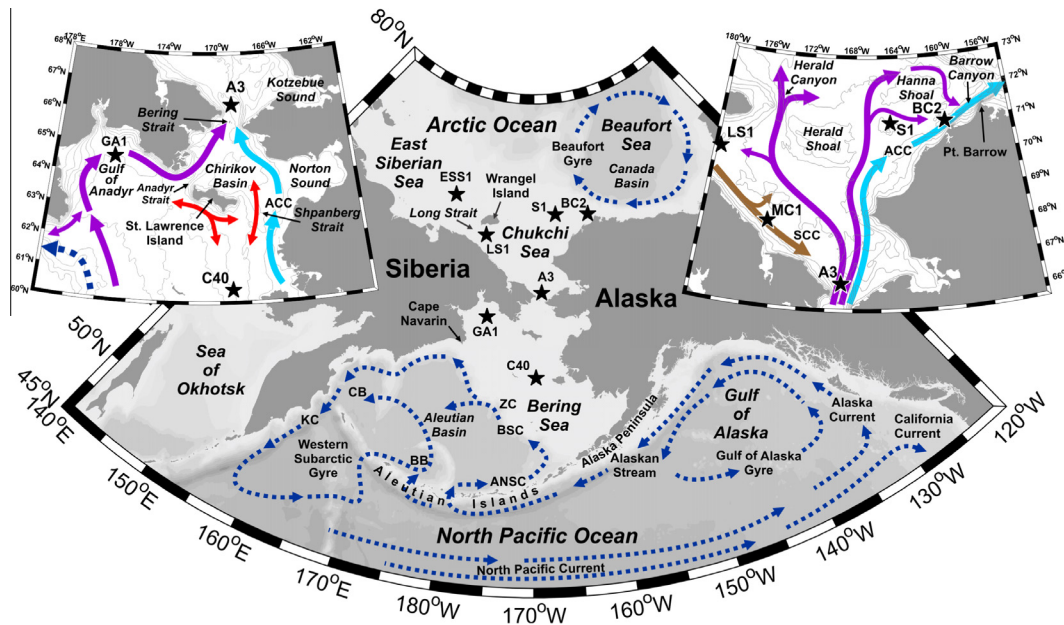
Fig. 1. Western Arctic and North Pacific place names, shaded bathymetry, circulation features, and locations (stars) of moorings A3, BC2, C40, MC1, and S1 along with reference sites LS1, GA1 and ESS1. Insets provide details of the northern Bering continental shelf/Bering Strait region (left) and the Chukchi Sea (right). Bathymetric contours on the insets are drawn at 10 m, 20 m, 30 m, 40 m, 50 m, 70 m, 100 m, 150 m, 200 m, 500 m, 1000 m, 2000 m, and 3000 m depth levels. Abbreviations include: ACC = Alaskan Coastal Current; SCC = Siberian Coastal Current; KC = Kamchatka Current; BSC = Bering Slope Current; ANSC = Aleutian North Slope Current; BB = Bowers Basin; CB = Commander Basin; ZC = Zhemchug Canyon.

scales over which these winds are important. Our approach considers how the effects of both long-term (inter-annual) and short-term (synoptic; hours to days) atmospheric variations reinforce or oppose each other to determine the net Bering/ Chukchi shelf circulation field.

1.2. Importance of Bering Strait

The Bering and Chukchi seas are linked by the narrow (85 km) and shallow (50 m) Bering Strait, through which the North Pacific communicates with the Arctic (Fig. 1). The net northward transport of Pacific waters through Bering Strait extensively affects Arctic sea ice (Aagaard et al., 1981; Paquette and Bourque, 1981; Shimada et al., 2006; Woodgate et al., 2010), the global hydrologic cycle (Aagaard and Carmack, 1989; Wijffels et al., 1992; Serreze et al., 2006; Stigebrandt, 1984), and the global thermohaline circulation (Shaffer and Bendtsen, 1994; Goose et al., 1997; Wadley and Bigg, 2002; De Boer and Nof, 2004a,b; Hu et al., 2010). These waters also carry carbon, nutrients, and plankton that sustain the enormously productive northern Bering–Chukchi ecosystem (Grebmeier et al., 1988; Walsh et al., 1989; Springer and McRoy, 1993). Hence, an understanding of the dynamics, properties, and fate of the transport through Bering Strait is essential to studies of these ecosystems.

1.3. Wind and the regional subtidal circulation

The winds over the Bering and Chukchi seas depend upon the time-varying strength and position of the Siberian and Beaufort highs and Aleutian Low atmospheric pressure systems. Moreover, in the North Pacific the cyclonic wind stress curl of the Aleutian Low forces both the Western Subarctic (Isoguchi et al., 1997; Pickart et al., 2009) and Gulf of Alaska gyres (Wilson and Overland, 1986; Lagerloef, 1995). In the Arctic, the anticyclonic curl of the Beaufort High drives the Beaufort Gyre (Proshutinsky and Johnson, 1997; Proshutinsky et al., 2002).

Despite the annual mean winds being northerly (blowing from the north) in the Bering Strait (Woodgate et al., 2005a), the

long-term (mutli-decadal) mean transport through the Bering Strait is ~0.8 Sv northward (Ratmanov, 1937; Shtokman, 1957; Coachman et al., 1975; Coachman and Aagaard, 1981, 1988; Roach et al., 1995; Woodgate et al., 2005b). It has long been argued that this flow is maintained by an along-strait sea surface slope of ~10^{-6} (Shtokman, 1957; Coachman and Aagaard, 1966; Coachman et al., 1975), and Stigebrandt (1984) and Aagaard et al. (2006) have proposed a corresponding steric height difference between the Arctic and North Pacific oceans of ~0.7 m relative to 800 db.

Transport variations are substantial, however, and occur on timescales from hourly to interannual, and likely longer (Bloom, 1964; Fedorova and Yankina, 1963; Coachman and Aagaard, 1966, 1981; Coachman et al., 1975; Coachman and Aagaard, 1981; Aagaard et al., 1985; Coachman and Aagaard, 1988; Roach et al., 1995; Woodgate et al., 2005a,b, 2006, 2010, 2012). The maximum monthly mean northward transport is typically in summer, when winds are weak (Aagaard et al., 1985; Woodgate et al., 2005b), and minimum monthly mean northward transport in winter, when there are more storms. Indeed, particularly strong northerly winds can reverse the transport for periods of days to weeks (Coachman and Aagaard, 1981; Woodgate et al., 2005a,b).

Linear regressions using local winds (generally taken within 150 km of the strait), atmospheric pressure, or atmospheric pressure gradients account for about half of the observed subtidal Bering Strait transport variance in winter and one-fourth in summer. These regressions include a constant term that is often assumed to represent the Pacific–Arctic pressure head (Coachman and Aagaard, 1981, 1988; Aagaard et al., 1985; Cherniawsky et al., 2005; Woodgate et al., 2005a, 2012), but the causes and magnitude of fluctuations in this term are not well known. In addition, the distinction between "local" and "regional" wind forcing is not always clear, in part because the wind records are often taken from relatively coarse atmospheric models. As we will show, a significant fraction of the strait transport variability is forced by continental shelf waves generated by winds well outside the strait region (defined herein as the Chirikov Basin and the southern Chukchi Sea).

The waters entering Bering Strait primarily originate over the Bering Sea shelf and continental slope. Upwelled slope waters flow onshelf through the Gulf of Anadyr (Coachman et al., 1975; Sambrotto et al., 1984) in accordance with arrested topographic wave dynamics (Kinder et al., 1986). Some of these waters thence flow eastward south of St. Lawrence Island (Schumacher et al., 1983; Danielson et al., 2006), although the bulk continues northward through Anadyr Strait (Fig. 1). Indeed, Overland and Roach (1987), Muench et al. (1988), and Clement et al. (2005) have all suggested that the Anadyr Strait throughflow comprises ∼80% of the mean Bering Strait transport.

Winds over the Bering shelf can redistribute the onshelf flow via Ekman transport, however (Danielson et al., 2012a). In particular, southerly and southeasterly winds over the Bering shelf drive coastal convergence along the Alaska coast, accelerate quasi-geostrophic shelf currents northward, and increase the flow through Shpanberg Strait (Johnson and Kowalik, 1986; Danielson et al., 2012b). Indeed, very limited observations and numerical models suggest that occasionally Bering Strait is fed wholly through Shpanberg Strait, while the Anadyr Strait flow reverses to the west (Muench et al., 1988; Danielson et al., 2012a). In contrast, northerly and northwesterly winds over the central Bering shelf result in coastal divergence and force shelf currents southward. These events often reverse the flow in Shpanberg Strait, and, if sufficiently strong, may be associated with flow reversals in Bering Strait as well (Danielson et al., 2012b).

North of Bering Strait, sea floor topography directs flow along three main features: Herald Canyon in the west, Barrow Canyon in the east, and the Central Channel between them (Winsor and Chapman, 2004; Weingartner et al., 2005; Woodgate et al., 2005a; Spall, 2007). Here again flow variations are largely wind-forced (Mountain et al., 1976; Weingartner et al., 1998, 2005; Woodgate et al., 2005a), although the wind-current correlation is notably smaller near Herald Canyon and along the Siberian coast (Woodgate et al., 2005a; Pickart et al., 2009).

1.4. Objectives and organization

We here develop a conceptual model that relates wind forcing over the North Pacific and western Arctic to the Bering–Chukchi shelf circulation. In particular, we show that variations in the position and strength of the Aleutian Low and the Beaufort High drive shelf and basin adjustments that together control much of the shelf circulation, including the Bering Strait throughflow. The analyses provide insights into the observed seasonal decoupling of winds and regional currents, the role of continental shelf waves on synoptic-scale transport fluctuations in Bering Strait, and the link between changes in the along-strait pressure gradient due to Ekman pumping over the Aleutian Basin and coastal divergence in the Arctic, both at interannual and shorter time scales.

The paper is arranged as follows. Section 2 describes the data sets, numerical models, and atmospheric reanalysis products used. Section 3.1 summarizes inter-annual, seasonal, and synoptic variability in the atmospheric forcing. Section 3.2 examines time-averaged depictions of the flow field. Sections 3.3 and 3.4 address the influence of continental shelf waves and the sources of variability in the meridional pressure gradient. Discussion and conclusions are in Sections 4 and 5.

2. Data and methods

2.1. Current meter data

The mooring data are derived from numerous observational programs spanning various years from 1979–2010 and carried out by the University of Alaska Fairbanks (UAF), the University of Washington (UW), and the Pacific Marine Environmental Laboratory (PMEL). Data from instruments deployed before 2000 (and subsequently to a lesser extent) were collected with mechanical current meters (RCMs), with the exception of acoustic Doppler current profilers (ADCPs) on two moorings in 1998–1999 in the St. Lawrence Island polynya (SLIP). Current records from the Bering shelf during the 1970s–90s were downloaded from the PMEL database (http://www.epic.noaa.gov/epic/) and PMEL ADCP mooring data from the 70 m isobath on the Bering Sea shelf from the University Corporation for Atmospheric Research Earth Observing Laboratory (UCAR-EOL) data archive (http://www.eol.ucar.edu/projects/best/). Bering Strait mooring data are from the UW Applied Physics Lab (UW-APL) Bering Strait data archive (http://psc.apl.washington.edu/BeringStrait.html, also available at the National Ocean Data Center (NODC) and UCAR-EOL), while UAF and UW Chukchi Sea mooring records from the 1990s and the SLIP and Bering Ecosystem Study (BEST) program deployments from 2008–2010 are held in archives at UAF, NODC, and UCAR-EOL. The RCM records were inspected for periods of stuck rotors or biofouling, and questionable data were discarded. All current meter data were detided with a 6th order 35-h cutoff low-pass Butterworth filter. The mooring sites, deployment lengths, and associated statistics are tabulated in Appendix A.

We pick three mooring sites at which to examine currents in some detail and compare these to numerical model results: C40, S1, and A3 (Fig. 1 and Table 1). Measurements at the central Bering shelf (C40) (Danielson et al., 2012b) and the northeast Chukchi shelf (S1) mooring sites used here extend from October 2008 through September 2009.

Mooring site A3 (Fig. 1) comprises one element of the contemporary Bering Strait mooring array, and its record is used here because it has been occupied continually since 1997 (Woodgate et al., 2005b, 2012). Furthermore, the A3 velocity record is strongly correlated ($r > 0.9$) with velocities measured at other sites in the strait (Coachman and Aagaard, 1981; Woodgate et al., 2005b) and has therefore been used as a basis for calculating the total Bering Strait transport (e.g., Woodgate et al., 2005b, 2006, 2010, Woodgate et al., 2012). Transport uncertainties based on A3 are ∼20% (Woodgate et al., 2005b) due to unmeasured vertical shears and horizontal variations associated with the buoyancy-forced and seasonally varying Alaskan Coastal Current (ACC) (Coachman et al., 1975; Gawarkiewicz et al., 1994; Woodgate et al., 2005b), and also to episodic southward intrusions of the Siberian Coastal Current (SCC) (Weingartner et al., 1999). We use the A3 ADCP mid-depth bin closest to 33 m to construct our A3 time series. Prior to 2007, RCM instruments at A3 were deployed at ∼48 m, and to correct for the water column shear shown by the ADCPs, we have increased the 1997–2006 RCM speeds by 10%. Because the A3-based transport estimates are based on a simple linear scaling of velocity with the Bering Strait cross-sectional area, the through-strait velocity and transport terminology are interchangeable for our purposes, within the caveats noted above.

2.2. CTD profile data

North Pacific Conductivity–Temperature–Depth (CTD) profile data were downloaded from the World Ocean Database for the years 2000–2012 (Boyer et al., 2009). Profiles from both ship-based platforms and from ARGO profiling floats from the Aleutian Basin were used to compute dynamic heights using the Ocean Data View (ODV) software package version 3.3 (Schlitzer, 2002). Dynamic height values (referenced to 800 dbar) that exceeded five standard deviations were removed.

Table 1
Summary of current meters used in the modeled-observed current comparisons. RCM instruments on A3 were deployed at ∼48 m depth prior to 2007, and their velocities were adjusted to match the 33 m depth ADCP measurements as described in Section 2.1.

Institution & project	Instrument type	Site name	Longitude	Latitude	Bottom depth (m)	Measurement depth	Years
UAF/UW Bering Strait	ADCP and RCM	A3	168.97°W	66.33°N	58	33 m	1997–2011
ConocoPhillips/Shell Chukchi Sea Environmental Studies Program	ADCP	S1	165.00°W	71.00°N	38	26 m	2008–2009
UAF/UW BEST	ADCP	C40	169.02°W	60.34°N	41	5–32 m Vertical average	2008–2010

2.3. Satellite altimetery data

Monthly mean gridded satellite altimetry data were downloaded from the Aviso (http://www.aviso.oceanobs.com) distribution center, which combines data from the Topex/Poseidon mission along with other satellites to generate global gridded sea surface height (SSH) anomalies from December 1992 to the present ($N = 252$ months). The merged data are gridded to a $1/3° \times 1/3°$ Mercator grid and available at monthly intervals. Aviso processes these data following the procedures given by CNES (2013). This processing also includes an extended Low Resolution Mode (LRM) and a Doppler/Synthetic Aperature Radar (SA) pseudo-LRM mode, which allow extended high latitude coverage over seasonally ice-covered shelves (CNES, 2013). Expected accuracy (<2 cm) is <5% of the signal variance for multi-satellite month-long averages (Le Traon and Dibarboure, 1999), but variance increases in seasonally ice-covered waters and many grid cells therefore contain no usable data. We removed the annual cycle by subtracting each month's mean at each grid cell from the appropriate time steps.

Although altimeter data are spotty and noisy in regions of sea ice, on average the data set provides SSH anomalies for 6 months per year within the Beaufort Gyre (defined as the sector bounded by 160°W, 130°W, 73°N and 80°N), from which we construct an annual time series. This series is biased toward summer and fall, but based on the gyre dynamics described by Proshutinsky et al. (2002), we expect that the gyre SSH anomaly decorrelation time scale is longer than the gaps between satellite estimates.

2.4. Three-dimensional circulation model

The Northeast Pacific (NEP) model, a 3-D regional circulation model based on the Regional Ocean Modeling System (ROMS), was used to diagnose the circulation over the Bering shelf as a function of wind direction. The NEP model is configured with ∼10 km horizontal resolution, 50 vertical (sigma coordinate) layers, and the domain extends ∼2000 km offshore from California in the south and thence northward to cover all of the Bering Sea and the southern Chukchi Sea (Curchister et al., 2005). The model is forced by realistic surface fluxes (Large and Yeager, 2009), coastal freshwater discharges (Dai et al., 2009), tides (Egbert and Erofeeva, 2002), and winds (Large and Yeager, 2009). It also includes a thermodynamic-dynamic sea ice module (Hunke and Dukowicz, 1997; Hunke, 2001; Mellor and Kantha, 1989; Roed and Debernard, 2004; Budgell, 2005). Boundary conditions are taken from the Simple Ocean Data Analysis (SODA) reanalysis, a global 0.5° ocean reanalysis product (Carton et al., 2000a,b; Carton and Giese, 2008). The NEP model has been compared to a wide variety of ice, temperature, salinity, and velocity records, including those from Bering Strait (e.g., Danielson et al., 2011b, 2012a). The run used here was integrated over 1987–2007, using model version NEP6.

2.5. Two-dimensional circulation model

Using the ROMS we also constructed a new barotropic model to examine the Bering/Chukchi shelf circulation when forced only with wind stress. This idealized model is run with uniform water density throughout, no surface or lateral heat or fresh water fluxes, no ice cover, no Pacific–Arctic pressure head, and no velocity or SSH variations imposed along the lateral boundaries. We refer to this model as the Alaska region vertically integrated (ARVI) model. The vertically integrated, nonlinear equations of motion for the east and north velocity components (u, v) describe a balance of the Coriolis force (f) with the horizontal pressure gradient due to SSH (ζ) variations, quadratic bottom friction (with coefficient $C_D = 3 \times 10^{-3}$), and wind stress (τ_x, τ_y). The ARVI model solves these equations of motion:

$$\frac{Du}{Dt} - fv = -g\frac{\partial \zeta}{\partial x} + \tau_x - C_D\frac{u(u^2 + v^2)^{1/2}}{H} \tag{1a}$$

$$\frac{Dv}{Dt} + fu = -g\frac{\partial \zeta}{\partial y} + \tau_y - C_D\frac{v(u^2 + v^2)^{1/2}}{H} \tag{1b}$$

where g is the acceleration due to gravity, $H(x,y)$ is the water depth, and D/Dt is the material derivative. The model domain spans approximately 156°E to 124°W and 50°N to 74°N at a horizontal grid resolution of ∼4 km. The bathymetric grid is derived from the Alaska Region Digital Elevation Model (Danielson et al., 2011b) between 45–64°N and the International Bathymetric Chart of the Arctic Ocean (Jakobsson et al., 2012) north of 64°N. Chapman–Flather radiation boundary conditions allow propagating disturbances to leave the domain at the shallow water phase speed $c = (gH)^{1/2}$ (Flather, 1976; Chapman, 1985).

Although the ARVI model is an idealization of the study region, it allows us to examine a reduced set of physics that avoids the complexities associated with stratification, fronts, ice, surface heat fluxes, coastal discharges, and intra-basin pressure heads. Because of the vertical averaging, we do not expect the model to perform well along the continental slope or in deeper waters, but rather to exhibit some skill over the shelf, particularly in winter, when horizontal and vertical density gradients are minimal due to the wind and convective mixing (e.g., Danielson et al., 2011a).

2.6. Atmospheric reanalyses

We represent synoptic, seasonal, and inter-annual variations in the atmospheric forcing with the North American Regional Reanalysis (NARR) (Mesinger et al., 2006), the Modern Era Regional Reanalysis (MERRA) (Rienecker et al., 2011), and the NCEP/NCAR Reanalysis 1 (NCEPR; Kalnay et al., 1996) wind and sea level pressure (SLP) fields. For example, we used daily NCEPR SLP fields to examine the structure and temporal variability in the atmospheric pressure systems over the study region (http://www.esrl.noaa.gov/psd). The NCEPR consists of 6-hourly realizations of major atmospheric variables on a 2.5° global grid. Output fields from

1948–2012 for the entire northern hemisphere poleward of 30°N allow retrospective analyses using daily means at each grid point for the 64-year time series. We computed 95% confidence limits to determine whether SLP anomalies were statistically different from the daily mean, conservatively assuming 63 effective degrees of freedom. This approach underestimates the number of synoptic degrees of freedom but neglects potential multi-year autocorrelations. Computation using the 64-year daily SLP record at site C40 reveals an integral time scale of 2–3 months (Emery and Thomson, 2001), showing that inter-annual autocorrelations are effectively masked by the greater variability associated with synoptic to seasonal variations.

The NARR model (Mesinger et al., 2006) computes winds on a ~35 km grid with 3 h time steps from 1979-present. The 10 m height wind vector components were downloaded from NOMADS, the National Climate Data Center's National Operational Model Archive & Distribution System (http://nomads.ncdc.noaa.gov:80/dods/NCEP_NARR_DAILY/narr-a_221_uvsfc.subset). We used NARR records to represent the wind field near current meter mooring sites C40, A3, S1, and BC2, and at site ESS1 in the East Siberian Sea, where there is no current meter record (Fig. 1).

Because the NARR grid does not cover the entire ARVI model domain and the NCEPR grid and time step are both relatively coarse, we used winds from NASA's MERRA reanalysis (Rienecker et al., 2011) to force the ARVI model. MERRA winds are hourly (which we subsampled to 3-hourly) at a horizontal resolution of 1/2° latitude and 1/3° longitude. Wind stress was computed from the MERRA winds following Large and Pond (1981), but the stress was not adjusted for air density changes. Test computations show that this simplification can underestimate the wind stress as much as ~20% in the Bering Strait region during winter and overestimate the wind stress by ~5% in summer.

3. Results

3.1. Regional atmospheric conditions: structure and variability

A useful coordinate transformation for Bering shelf winds is a counterclockwise rotation of 45° into the along- and cross-shelf directions (Danielson et al., 2012a). Hence, many of the analyses that follow are based on rotated winds wherein the along-shelf component $V_R > 0$ is toward 315°T (southeasterly winds) and the cross-shelf component $U_R > 0$ is toward 45°T (southwesterly winds), see Fig. 2a. An Aleutian Low centered over the Bering Sea basin typically generates southeasterly winds ($V_R > 0$) over the Bering shelf, but lows over the Gulf of Alaska tend to produce predominantly northerly and north–northeasterly winds ($V_R < 0$ and

$V_R = 0$). Following Danielson et al. (2012a,b) we select the NARR wind record from 60°N, 170°W (which is very close to the C40 mooring site) to represent wind conditions over the central Bering Sea shelf.

We first determine the associated atmospheric pressure fields that establish the two distinct Bering Sea along-shelf wind directions. In winter (October to April) the shelf experiences strong wind forcing, weak stratification, and swift, but highly variable currents (Kinder and Schumacher, 1981; Schumacher and Kinder, 1983; Stabeno et al., 2010; Danielson et al., 2012b). We group winter months according to whether $V_R > 0$ (along-shelf wind component directed to the northwest, Fig. 2b) or $V_R < 0$ (along-shelf wind component directed to the southeast, Fig. 2c), based on the NARR winds near C40. With respect to the monthly mean wind, these patterns are associated with an Aleutian Low centered over the Aleutian Basin ($V_R > 0$) or over the Gulf of Alaska ($V_R < 0$). On average, winds with $V_R > 0$ are also associated with an enhanced Beaufort High, whereas winds with $V_R < 0$ correspond to an enhanced Siberian High.

We then examine temporal changes in the patterns shown in Fig. 2 using pressure reference points A–D located at the corners of the region bounded by 170°E, 150°W, 57.5°N, and 70°N (Fig. 3 and Table 2). The SLP gradients $\Delta_1 = SLP(A) - SLP(D)$ and $\Delta_2 = SLP(B) - SLP(C)$ are used to define the regional atmospheric pressure field with respect to a threshold value for changes, T, which is taken as one standard deviation of the daily mean SLP at the 60°N, 170°W reference point ($T = 14$ millibars; 1 millibar = 100 Pa). The parameters Δ_1, Δ_2, and T allow us to identify the fraction of time the North Pacific and western Arctic atomospheric fields would promote strong or weak $V_R < 0$ and $V_R > 0$ conditions and the associated mean SLP structure. In particular, using the definitions shown in Table 2 there exist seven distinct configurations of Δ_1, Δ_2, and T that together account for all atmospheric conditions. Based on the daily mean NCEPR SLP fields, Fig. 3 shows the mean SLP associated with each of the seven pressure patterns during winter along with the fraction of time that each occurs. Colored regions in Fig. 3 show that the Bering shelf wind field variations represent responses to the large-scale northern hemisphere atmospheric circulation, and that many areas far beyond our domain of interest reorganize in concert with the identified patterns.

Seasonal variability is pronounced, with most patterns appearing at different frequencies in summer and winter (Table 2). For example, pattern P6 captures the summer increase of Arctic cyclone activity (Reed and Kunkel, 1960; Serreze et al., 1993).

Given our understanding of the Bering shelf response when subjected to winds of varying direction (Danielson et al., 2012a,b), we can ascribe expected oceanic responses to each panel
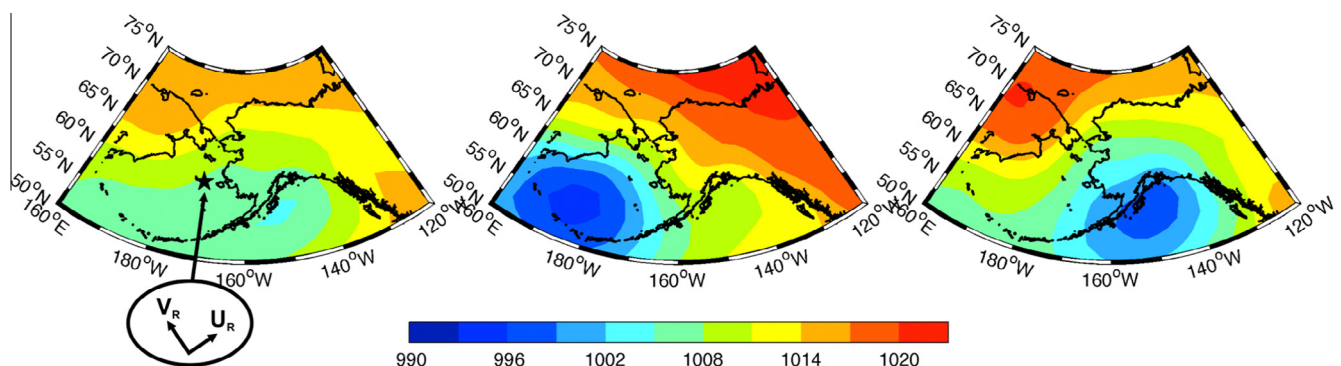
Fig. 2. The 1979–2012 October–April mean NCEPR SLP field (millibars) under all wind conditions (left), $V_R > 0$ (center), and $V_R < 0$ (right). Winds are from NARR at reference point 60°N, 170°W (star), where V_R is the monthly mean along-shelf velocity component, oriented toward 315°T for $V_R > 0$ (see left-hand panel). The $V_R > 0$ panel exhibits a westward displaced Aleutian Low and an enhanced Beaufort High; the $V_R < 0$ panel exhibits an eastward displaced Aleutian Low and an enhanced Siberian High.
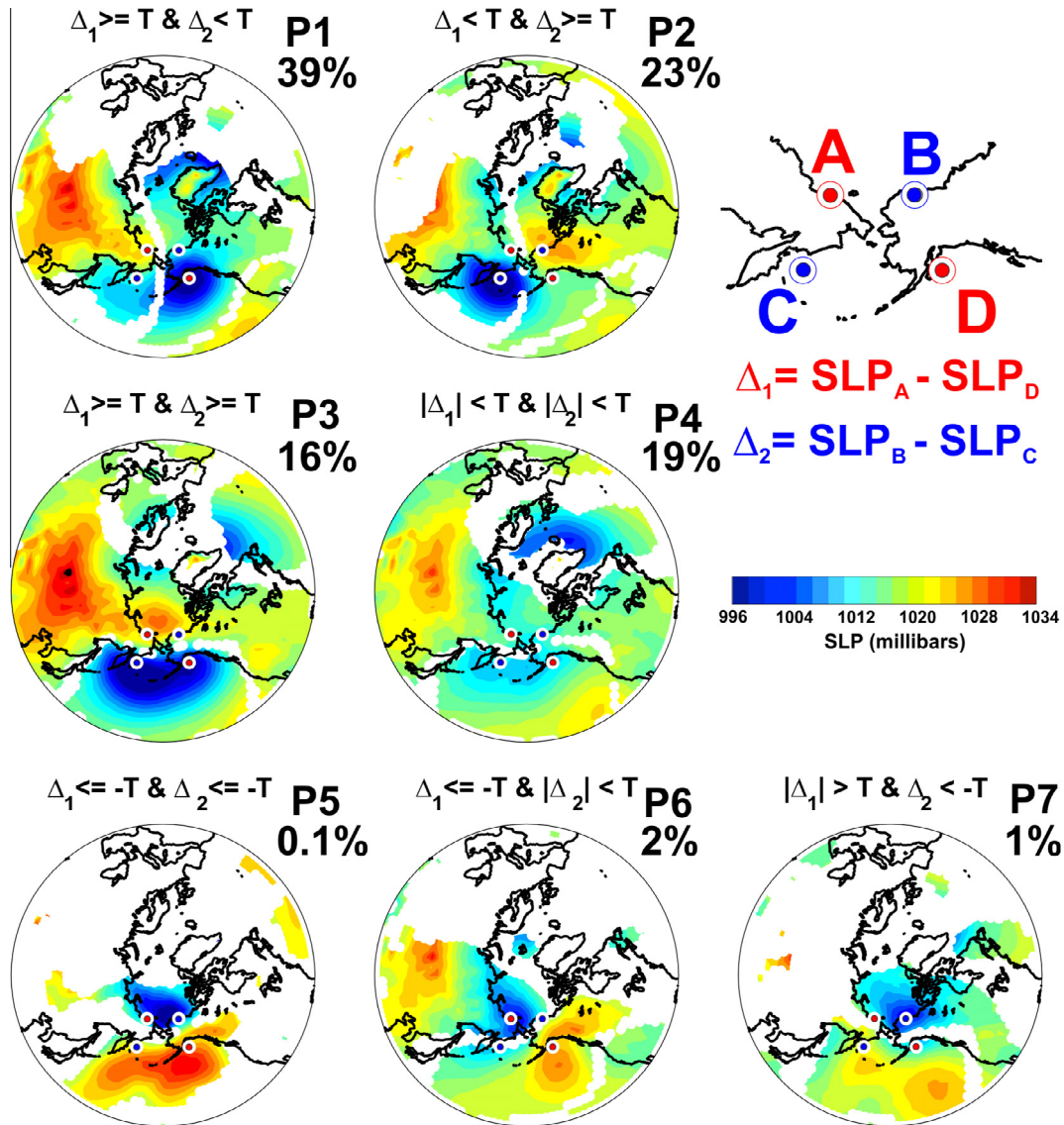
Fig. 3. SLP patterns P1–P7 for October–April based on 1948–2012 daily NCEPR SLP fields as defined by the relations shown for SLP gradients Δ_1, Δ_2, and threshold $T = 14$ millibars. Grid points at which the SLP is statistically different from the October–April mean are colored. Percentages denote the fraction of days from October–April that each pattern is present. Each pattern's spatial structure remains essentially unchanged in summer months, but the fraction of time that each pattern manifests does change (see Table 2). Interannual variability in the prevalence of pattern P1 are shown in Fig. 4.

Table 2
Summary of SLP patterns shown in Fig. 3, giving the SLP pressure pattern number; the numerical definition for each pattern; the mean fraction (percent) of days that the NCEPR daily SLP fields accounted for each pattern during October–April (O–A) and May–September (M–S); and mean conditions associated with each pattern. The SLP gradient change threshold is taken as $T = 14$ millibars (1 millibar = 100 Pa).

Pressure pattern #	Definition	O–A (%)	M–S (%)	Characteristics
P1	$\Delta_1 \geqslant T$ and $\Delta_2 < T$	39	11	Strong east-displaced Aleutian Low and enhanced Siberian High
P2	$\Delta_1 < T$ and $\Delta_2 \geqslant T$	23	13	Strong west-displaced Aleutian Low and enhanced Beaufort High
P3	$\Delta_1 \geqslant T$ and $\Delta_2 \geqslant T$	16	1	Strong centrally located Aleutian Low
P4	$|\Delta_1| < T$ and $|\Delta_2| < T$	19	65	Weak regional SLP gradients
P5	$\Delta_1 \leqslant -T$ and $\Delta_2 \leqslant -T$	0.1	0.1	Strong North Pacific High and Arctic Low
P6	$\Delta_1 \leqslant -T$ and $|\Delta_2| < T$	2	7	East Siberian Sea Low and Gulf of Alaska High
P7	$|\Delta_1| > T$ and $\Delta_2 < -T$	1	3	Beaufort Sea Low and Bering Sea High

shown in Fig. 3. Pressure patterns P2, P3 and P6 (23%, 16% and 2%, respectively, in winter) all represent coastal downwelling conditions along the Alaskan Bering coast and promote northward flow anomalies over the central shelf. Patterns P1, P5 and P7 (39%, 0.1% and 1.0%, respectively) are upwelling-favorable and promote

southward flow anomalies. Pattern P4 (19%) shows little potential for appreciable wind-forced flow over the Bering and Chukchi shelves because SLP gradients are weak over both shelves.

We next compile the number of days when each pattern is dominant on an annual basis to consider inter-annual variability

in the wind forcing. Although there are no record-length trends, the dominant P1 pattern (and also P2, which is inversely correlated with P1) tends to persist for several years (Fig. 4a). Fig. 4b and 4c show the fraction of time that the winds at C40 are directed along-shelf toward the southeast and 4d shows the winter wind direction anomaly with respect to the vector mean winter wind direction. The mid-1970's regime shift (Overland et al., 1999) stands out as a transition period from higher occurrences of P1 in the early part of the decade to fewer occurrences after 1977. An even more distinct transition occurred between 2005 and 2006. In 2005, the downwelling-favorable pressure patterns over the Bering shelf that dominated the first half of the decade were replaced with a larger fraction of upwelling-favorable pressure patterns that persisted through at least 2011. These changes all correspond to longitudinal shifts of the Aleutian Low, such that positive P1 anomalies are associated with a predominance of storms in the Gulf of Alaska.

Recent consecutive years of warm (2001–2005) and cold (2006–2010) ocean temperature anomalies (Overland et al., 2012; Stabeno et al., 2012) are consistent with the advective response of the Bering shelf to longitudinal displacements in the Aleutian Low (Danielson et al., 2011a, 2012a). Over the 1948–2012 NCEPR record, the 2005–2011 period is the only string of seven consecutive years of similarly signed anomalies in the upwelling-favorable P1 pattern. In addition, we note that the fraction of time that $V_R < 0$ in each of the 2005–2011 winters is greater than in any winter during 1995–2004.

Interestingly, the 2001–2005 warm period followed by the 2006–2011 cold period also corresponds to periods of low and then high annually averaged Bering Strait transport (Woodgate et al., 2012). The sign of the transport anomaly is puzzling in light of the results of Danielson et al. (2011a,b), that northward flow anomalies on the Bering shelf are associated with the downwelling-favorable southeasterly winds that occur when the Aleutian Low is displaced to the west. Given the latter results we might have

expected that the 2000–2005 period would have been associated with positive (northward) transport anomalies in Bering Strait. Before addressing this issue in Section 3.4, however, we first consider atmospheric and oceanic variability and co-variability from daily, monthly, and seasonal perspectives.

We assess the covariance in winds near sites C40, A3, S1 and ESS1 using the 1979–2012 NARR reanalysis. During this time, mean wind speeds are statistically different from one another ($p < 0.01$) and decrease with distance from C40; e.g., mean speed at C40 = 6.4 m s^{-1}, at A3 = 5.7 m s^{-1}, at S1 = 3.9 m s^{-1}, and at ESS1 = 3.5 m s^{-1}. Time series at these sites (Fig. 5) for October 2008 through October 2009 show that many of the events recorded at any given site are not closely mirrored at the other sites, even if nearly coincident events do occur at times. Fig. 6 shows the rotary coherence-squared (γ^2) relations of the winds at the four sites. Maximum $\gamma^2 \sim 0.4$ for periods of one month or longer, and occurs for pairs C40:A3, A3:S1 and S1:ESS1. Sites C40 and A3 winds are the most coherent, with $\gamma^2 > 0.2$ for periods longer than ~3 days, while C40 and A3 are only weakly coherent with winds at ESS1 ($\gamma^2 < 0.2$). The phase relation (not shown) reveals that winds at the southern sites tend to lead those at northern sites at daily to fortnightly periods, which is consistent with atmospheric lows propagating northeastward. At periods <4 days, C40 winds over the central Bering shelf are incoherent with S1 winds in the northeast Chukchi. The spatial differences in the coherence structure of the winds, and in the wind strength (Fig. 5), suggest that we look for spatially varying oceanic responses to wind forcing within the study region.

3.2. Northern Bering shelf response to wind direction

To understand current variations in Bering Strait and the Chukchi Sea, we first assess the circulation over the northern and central Bering shelf. We generate composites (Fig. 7) of the 3-D NEP6 model monthly mean vertically-averaged velocity fields for the
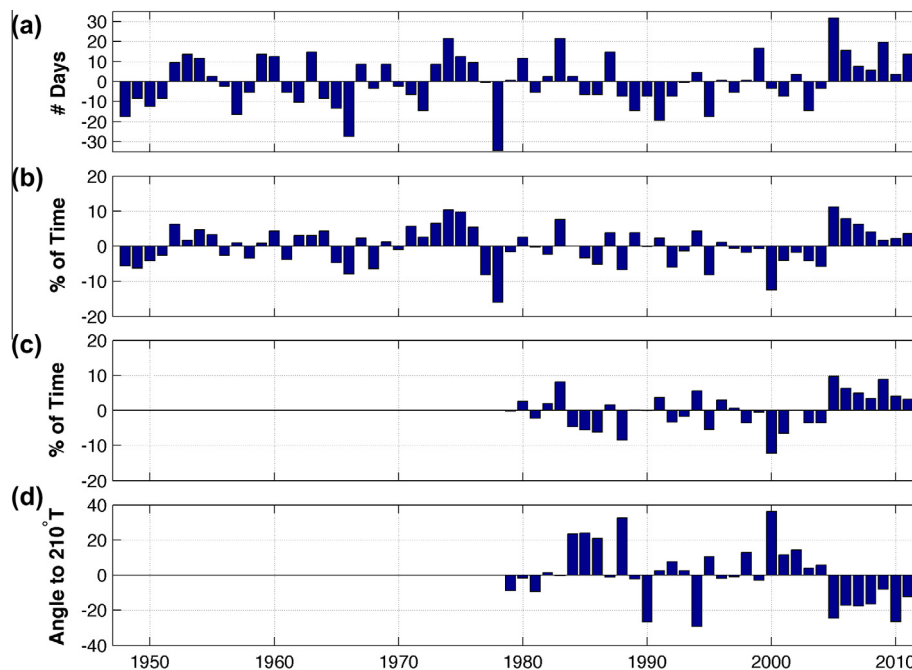
Fig. 4. Time series of winter (October to April) Aleutian Low longitudinal annual variability during 1948–2012. Panel (a) shows the anomaly in the number of days of the NCEPR P1 pressure pattern; (b) the anomaly in the percent of time that the NCEPR wind time series at C40 exhibited $V_R < 0$; (c) the anomaly in the percent of time that the NARR wind time series at C40 exhibited $V_R < 0$; and (d) the winter wind direction anomaly in the NARR wind time series at C40 with respect to the mean winter wind direction (210°T). Each record depicts the transition from a centrally or westward located winter Aleutian Low in 2000–2005 to an eastward-displaced winter Aleutian Low after 2005.
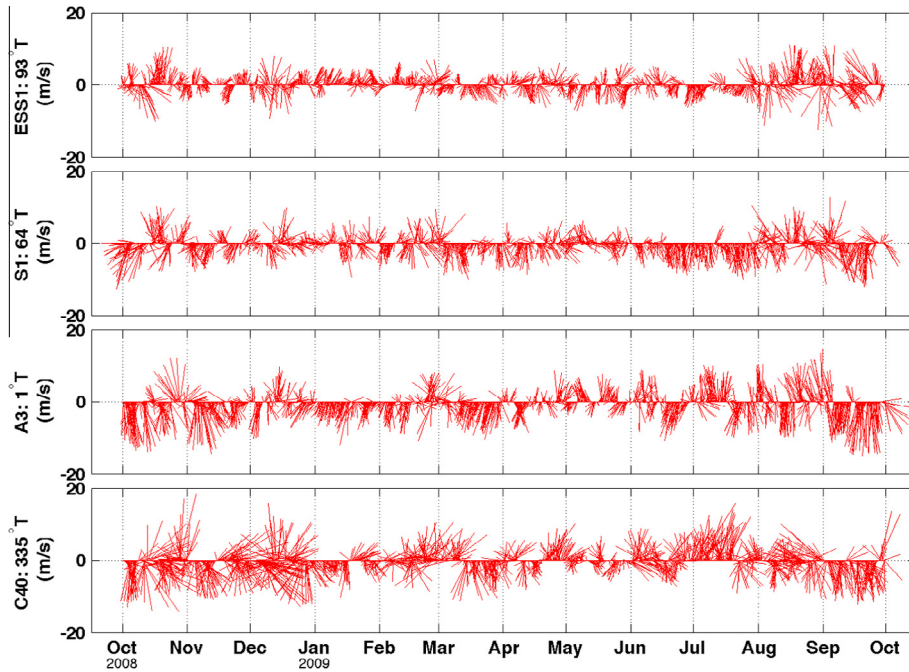
Fig. 5. Wind vectors every 6 h from NARR grid points near sites C40, A3, S1, and ESS1 from October 2008–September 2009. Vectors are rotated so that the principal axis of variation for each record (angle as marked) is directed along the ordinate axis.
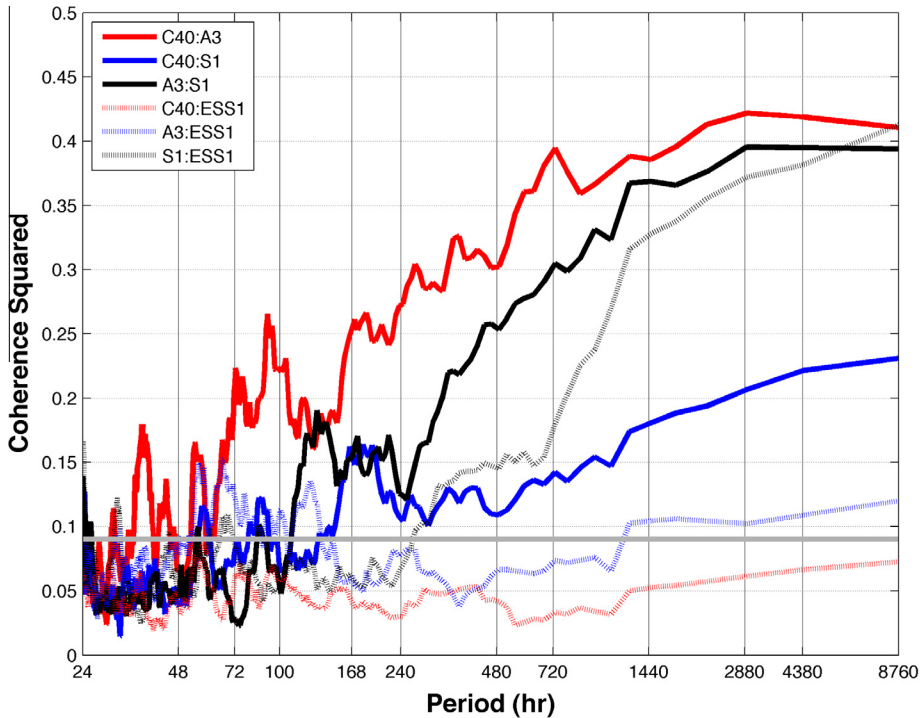

Fig. 6. Rotary coherence-squared between winds at C40, A3, S1 and ESS1, based on the 1979–2012 NARR reanalysis. Computations employ a 1-year Hanning window with no overlap; results are subsequently smoothed with a 15-point moving average to reduce noise. Following Thompson (1979) and using $n = 33$ yearlong windows to compute the level of significance gives a coherence-squared significance level of $\gamma^2 = 0.09$ (gray line).

long-term mean (Fig. 7a), the summer mean (Fig. 7b), the winter mean (Fig. 7c), and for winter months distinguished by the same wind criteria that delineate the panels of Fig. 2 (Fig. 7d).

Although the northern Bering Sea circulation is stronger in summer than winter (cf. Fig. 7b and c), the same basic circulation pattern holds in both seasons. In the winter case for which $V_R > 0$ (Fig. 7d) there is strong northward flow across much of the central

shelf, a large fraction of the Bering Strait throughflow originates east of St. Lawrence Island (within and/or south of Shpanberg Strait), off-shelf (westward) flow extends past Cape Navarin, and outer shelf currents over the 200 m isobath are generally directed to the northeast and cross isobaths. In contrast, for the winter case in which $V_R < 0$ (Fig. 7e) the flow is weak and southward in Shpanberg Strait, so that the northward Bering Strait throughflow passes
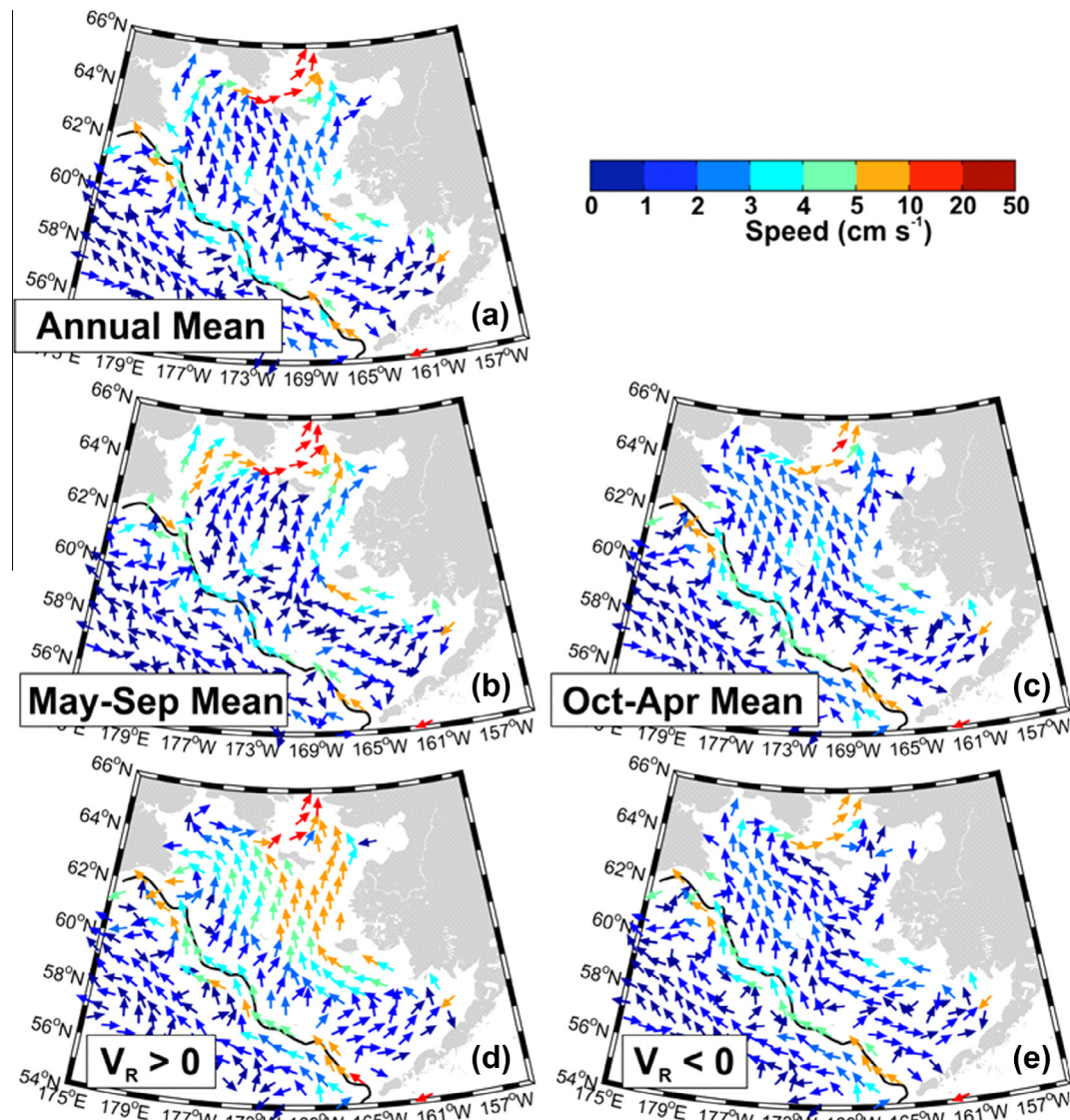
Fig. 7. Water column averaged currents from the 3-D NEP6 model. Panel (a) shows the average for the entire 1987–2007 hindcast, (b) the May–September average, (c) the October–April average, and (d and e) the October–April vertically averaged currents segregated into months for which (d) $V_R > 0$ and (e) $V_R < 0$. The black contour is the 200 m isobath.

entirely through Anadyr Strait, having originated in the on-shelf flow into the Gulf of Anadyr. On the shelf southeast of the Pribilof Islands the flow is southeastward, but over the outer shelf north of Zhemchug Canyon (Fig. 1) the flow is northward (and against the wind). Note in particular that this broad northward flow over the outer shelf converges in the Gulf of Anadyr, where it turns northeastward and feeds Anadyr Strait.

Examining the monthly mean transport time series (not shown) from the NEP6 model hindcast, we find that the northward transport through Anadyr Strait exceeds that in Bering Strait ~50% of the time, although on average the mean transport through Anadyr Strait is only ~80% of that in Bering Strait. Moreover, the monthly mean transport in Anadyr Strait reverses direction ~6% of the time (15 out of 252 months), whereas reversals occur 9% (22 months) of the time in Bering Strait and 30% (74 months) in Shpanberg Strait. Although the monthly averaged transports are uncorrelated between Anadyr and Shpanberg straits, both Anadyr ($r = 0.85$, $p < 0.01$) and Shpanberg ($r = 0.62$, $p < 0.01$) transports are significantly correlated with Bering Strait transports. Hence, Chirikov Basin represents an oceanic switchyard, whereby flows through

the three adjoining straits maintain continuity by adjusting to the greater shelf circulation and forcing (Muench et al., 1988; Coachman, 1993).

The Bering Strait transport is well correlated with winds in winter months, but not with the weaker winds of summer (Coachman, 1993; Cherniawsky et al., 2005). This quandary is partially resolved by examining the on-shelf flow through the Gulf of Anadyr under $V_R < 0$ and $V_R > 0$ conditions in summer vs. winter. The NEP6 realization of cross-shelf transport into the Gulf of Anadyr in winter (see also Fig. 4 of Danielson et al. (2012a)) shows that $V_R > 0$ is associated with off-shelf transport (Fig. 7d), but $V_R < 0$ with on-shelf transport (Fig. 7e). In summer, however, both wind conditions are associated with on-shelf transport (Danielson et al., 2012a). Typical June wind stress is about 0.05 Pa, whereas in December the average wind stress nearly triples to 0.13 Pa (wind stress is computed following Large and Pond (1981) based on the 3-hourly NARR timeseries at C40). Computing the associated surface Ekman transport across a shelf of length 1000 km, we find that the typical wind stress in June can force ~0.4 Sv, or only ~30% of the June Bering Strait flow (Woodgate et al., 2005b). The mean

summer wind stress is therefore incapable of overcoming the topographic beta vorticity constraints (Kinder et al., 1986) and shifting the waters destined for Bering Strait from Anadyr Strait to Shpanberg Strait (Danielson et al., 2012a). In contrast, the typical December wind stress drives an Ekman transport over the same 1000 km of ~1.0 Sv, or ~200% of the mean December Bering Strait transport (Woodgate et al., 2005b). Thus, only the winter winds are normally strong enough to appreciably reconfigure the overall shelf circulation (Danielson et al., 2012a). In summer, therefore, the along-strait pressure head must provide primary control of the shelf circulation, resulting in an intensified and relatively invariant flow through the Gulf of Anadyr toward Bering Strait.

In addition to the seasonal change in mean wind stress over the Bering shelf, three other mechanisms may alter the wind-current relation. First, summer stratification on the Bering shelf weakens the current response to winds in waters below the mixed layer (Danielson et al., 2012b). In this connection, we note that most Bering Strait current measurements prior to 2005 were made within 20 m of the seafloor. Second, the northward baroclinic jet associated with the buoyant Alaskan Coastal Current strengthens in summer, contributing ~0.1 Sv to the total transport of ~0.8 Sv (Gawarkiewicz et al., 1994; Woodgate et al., 2005b). Third, variable winds generate continental shelf and coastal-trapped waves (Gill, 1982; Brink, 1998), and since the stratification and winds vary seasonally, so will the nature of the subinertial wave field. In Section 3.3 we address the effects of the barotropic continental shelf waves in the context of wind-driven currents. An assessment of coastal-trapped waves is beyond the scope of this work. These are more likely present in the stratified summer season than winter and their absence in our analysis may account for some of the dissimilarities in the summer and winter wind–current relationships.

3.3. Synoptic scale wind-driven currents

We here analyze winds, current records, and satellite altimeter data, together with the results of numerical model integrations, to examine synoptic scale responses of the Bering–Chukchi shelf circulation to wind variations.

Based on current meter records, it is clear that that the Bering–Chukchi shelf circulation shows two spatially systematic average structures associated with the two along-shelf wind directions (Fig. 8). We can characterize the responses as follows. On average, southeasterly winds ($V_R > 0$) force increased northward flow in Bering (>40 cm s^{-1}) and Shpanberg (>20 cm^{-1}) straits. Currents at mid-shelf sites, 100 km or more south of St. Lawrence Island, are generally directed northward along isobaths, while nearer to St. Lawrence, shelf waters branch toward the two adjoining straits. Northwesterly and northerly winds ($V_R < 0$) reduce the Bering Strait flow (<10 cm s^{-1}) at depth and may even reverse this flow near the surface. The currents along the continental slope, near the Pribilof Islands, and in Unimak Pass are relatively unaffected by the V_R-based selection criteria for these averages, however (see also Appendix A). These observations are in qualitative agreement with the composite maps of modeled monthly means in Fig. 7d and e.

There is a similar bi-modal response across much of the Chukchi shelf that suggests a remote forcing component from the Bering Sea (Fig. 8). Eastern and central Chukchi currents are 5–15 cm s^{-1} and directed nominally northward for $V_R > 0$ winds over the Bering shelf. In contrast, the Chukchi circulation field collapses to near-zero for $V_R < 0$ winds. These characterizations hold well except for the four westernmost Chukchi sites in Fig. 8 (one in Long Strait, two in Herald Canyon, and MC1 near the Siberian coast). We discuss these differences below.

Fig. 9 shows current observations from C40, A3, and S1 recorded between October 2008 and September 2009. All three sites exhibit a strong seasonality, with larger variance in winter months at all sites. Correlations at zero time lag of the velocity component along the principal axis of variation are small ($r \sim 0.4$) but statistically significant ($p < 0.05$) for the Bering shelf: Bering Strait (C40:A3) and Bering Strait:Chukchi shelf (A3:S1) pairs. For the C40:S1 pair, the correlation is also significant, but still smaller ($r \sim 0.2$), and then only for C40 currents leading S1 currents by 36 h.

These correlations and the low coherence of Bering/Chukchi winds at periods <3 days suggest that at synoptic time scales the currents in Bering Strait and the Chukchi Sea respond to continental shelf waves generated on the Bering shelf. The cross-shelf length scale for these waves is the external Rossby radius of deformation, $R = (gH)^{1/2}f^{-1}$, ~120–150 km for an inner shelf depth of 25–40 m, and the phase speed for wavelengths >R is $c \sim \alpha g f^{-1}$, where α is the bottom slope (Cushman-Roisin, 1994). For the Bering and Chukchi shelves α is 2–5×10^{-4}, giving shelf wave phase speeds of 1300–3100 km day^{-1}, implying that long waves can traverse these shelves in less than a day. Changes in coastline orientation along the wave path suggest that some of the wave energy may be scattered (Allen, 1976; Wilkin and Chapman, 1987; Wilkin, 1988), with perhaps only a portion of the energy propagating through Bering and Anadyr straits, whose widths are ~0.5R.

We use the barotropic ARVI model and idealized wind forcing to test our hypothesis. Initially the entire model domain is at rest and is then subjected to an increasing southeasterly wind stress that builds to 0.1 Pa within two days (Fig. 10c). The wind stress is spatially invariant and confined to the Bering shelf as far north as Bering Strait; no winds are applied over the Chukchi shelf. These winds generate a coastal setup (Fig. 10d) and a northward velocity pulse (Fig. 10e), which subsequently propagates along the Alaskan coast and arrives at Barrow Canyon and the western Beaufort Sea approximately 24 h after passing through Bering Strait (Fig. 10a). A companion experiment with northwesterly winds generates a velocity response opposite to the southeasterly wind case. In both instances, after the wind stress is removed, a weaker pulse of currents flows in the direction opposite to that of the initial wave, but this second wave front also propagates northward into the Chukchi Sea. The time scale for the propagation is consistent with continental shelf wave theory. Since the magnitude of the along-shore velocity of these long waves (and any shorter waves) is small for distances greater than R from the coast, the waves have small signatures over the western Chukchi shelf. This is consistent with the lack of response observed at the current meter moorings located near Wrangel Island (Fig. 8) and helps clarify the first EOF mode of Woodgate et al. (2005a), which depicts an east–west pattern of variability on the Chukchi shelf. Our interpretation here is that the eastern and western Chukchi currents do not tend to fluctuate synchronously because the e-folding cross-shelf decay scale of continental shelf waves implies that these waves do not extend far enough from the Alaskan coast to influence the western Chukchi.

Similarly, winds over the East Siberian Sea may generate shelf waves that propagate along the Siberian coast toward Bering Strait from the northwest (Fig. 10b). The SSH contours in Fig. 10b show that some of the energy of these waves spreads eastward to the Alaskan coast and thence propagates northward toward Barrow Canyon, while another portion continues southward through Bering and Anadyr straits.

We now look for evidence for shelf waves within the gridded satellite SSH record. We select one grid point in the coastal East Siberian Sea and another on the eastern Bering Sea shelf, and then regress the SSH anomalies from these two reference points against the SSH anomaly at all altimeter grid points within the domain shown in Fig. 11. We find that positively correlated signals extend downstream (in the Kelvin wave sense) along both coasts,
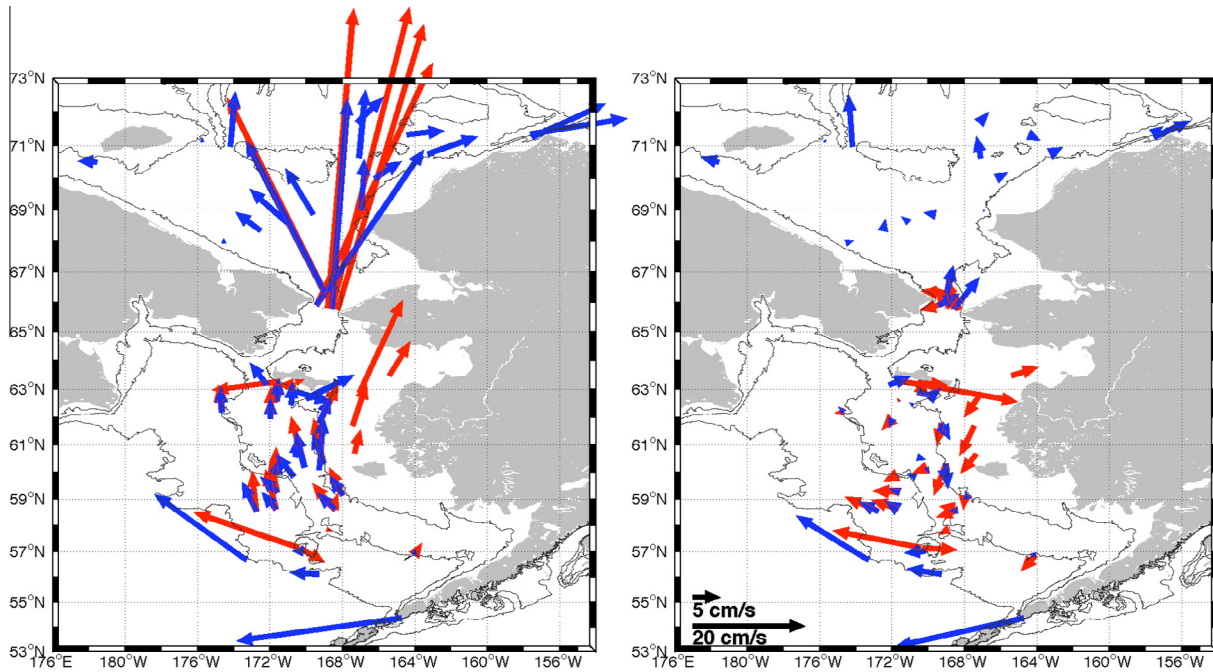
Fig. 8. Composite averages of 10–20 m depth (red) and 30–60 m depth (blue) currents over the Bering and Chukchi shelves for moored current meter observations made during October–April variously deployed over 1979–2010. The left-hand panel corresponds to $V_R > 0$ and the right-hand panel to $V_R < 0$, where V_R is the along-shelf wind velocity component oriented toward 315°T for $V_R > 0$. Averages are based on the wind direction near C40 (60°N/170°W) for the 24 h prior to each current observation; each vector represents at least 30 days worth of hourly observations. See Appendix A for additional details.
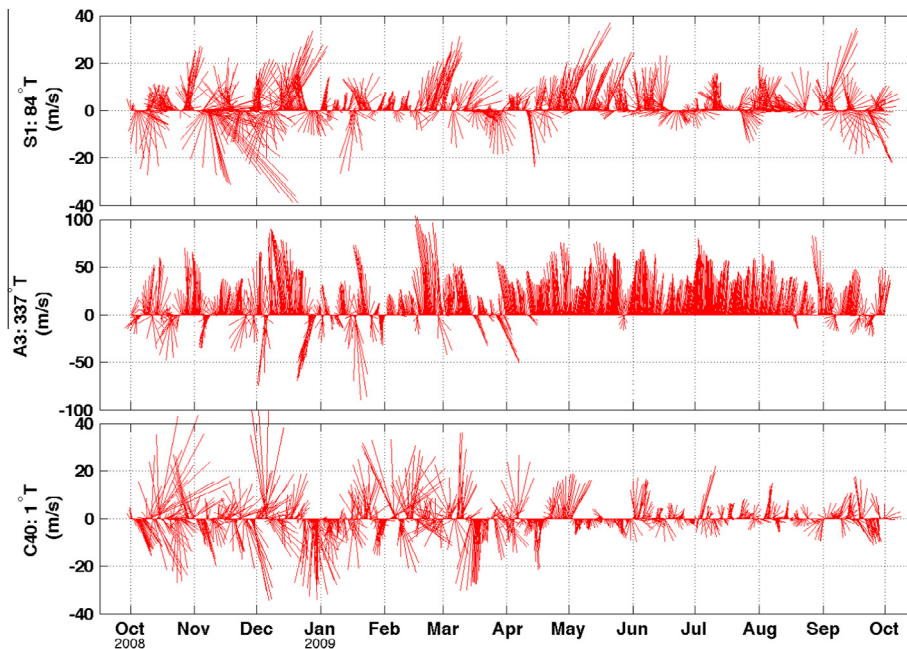

Fig. 9. Observed currents every six hours at moorings C40, A3, and S1 from October 2008–September 2009. Vectors are rotated so that the principal axis of variation (angles as marked) for each record is directed along the ordinate. See Fig. 6 for the accompanying wind time series at these sites.

consistent with the notion of shelf wave propagation northward from the Bering Sea to the northeastern Chukchi Sea along the Alaskan coast, and southward from the East Siberian and Chukchi seas through Bering Strait and into the Gulf of Anadyr. Moreover, the cross-shore decorrelation scale in SSH is generally 1–2R. In some places (e.g., the northern Chukchi Sea and southern/outer Bering shelf) the region of positively correlated anomalies may also

be influenced by the large (>200 km) atmospheric decorrelation length scales. If we assume that each month represents an independent sample of these synoptic-scale shelf waves, then $N = 252$ months and the correlation is significant ($r \geqslant 0.11$) even in the Gulf of Anadyr. Note that Bering Strait is so narrow that the southward-propagating waves along the Siberian coast overlap with northward-propagating waves along the Alaskan coast.
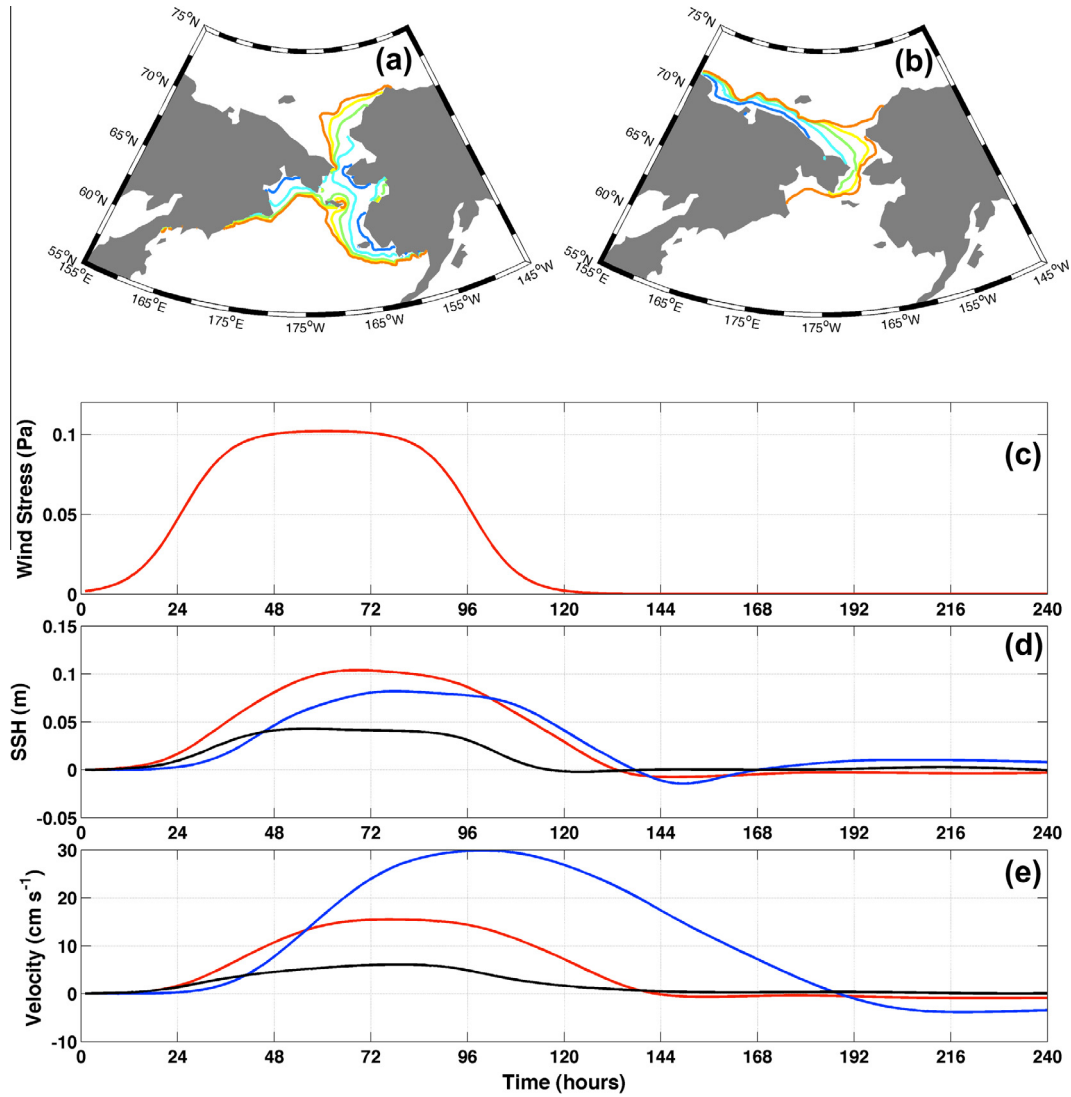
Fig. 10. Propagation times for continental shelf waves in the Chukchi Sea generated by the 2D vertically integrated ARVI model in the Bering Sea (a) and in the East Siberian Sea (b). Contours depict the 3 cm SSH isopleths at 24 (dark blue), 30 (light blue), 36 (green), 42 (yellow) and 48 (orange) hours after the integration start. Panel (c) shows the wind stress time dependency used to generate (a) and (b). For (a), spatially invariant winds blowing toward 315°T were applied only south of Bering Strait. For (b), winds were toward 120°T and applied only to the East Siberian Sea side of the 180th meridian. No winds were applied over the Chukchi Sea in either model run. Waves propagate away from the generation region with the coast on their right-hand side. The SSH and along-principal axis current velocity at A3 (red), BC2 (blue) and C40 (black) are shown in (d) and (e), respectively.
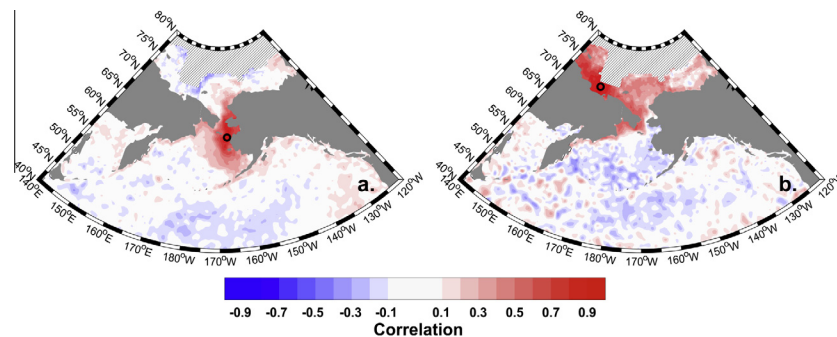
Fig. 11. Correlation of satellite-measured SSH anomalies with respect to the SSH anomaly at 167°W, 62.5°N in the eastern Bering Sea (left) and at 165°E, 71°N in the East Siberian Sea (right). Black circles locate the reference points. Sea ice cover precludes computations in the hatched region. The western Chukchi and East Siberian seas SSH anomalies do not co-vary with those in the eastern Bering Sea. Note the similarity in structure of the correlated regions to the shape of the contours shown in Fig. 10a and b, particularly with respect to the signals that extend around the Gulf of Anadyr and past Cape Navarin.

Idealized modeling of shelf waves under landfast ice (Kasper and Weingartner, 2012) suggests that a considerable portion of the East Siberian Sea shelf wave energy may be dissipated during months when extensive landfast ice is present, so that the response in Bering Strait to shelf waves generated in the East Siberian Sea may be muted through much of winter. The signals in Fig. 11 are biased toward summer months in areas of seasonal ice cover.

We also forced the barotropic ARVI model with MERRA winds to create a hindcast for December 2007 to July 2011 (denoted ARVI run #08) and compared the model results to observed currents at C40, A3 and S1 (Fig. 9). Fig. 12 shows the rotary coherence squared between the NARR winds at each of these sites and the observed currents, and between ARVI run #08 currents and the observed currents. The wind-current coherence is significant for some periods, but on average $\gamma^2 < 0.3$. In contrast, the ARVI model accounts for an appreciably greater fraction of the variance at all three sites, including $\gamma^2 \sim 0.6$ for the A3 mooring in Bering Strait (Fig. 9). Together, these results suggest that a large portion of the subtidal current variability on the Bering and Chukchi shelves can be accounted for by propagating continental shelf waves and local winds, with the former likely the more important. In this connection we note that the model-observation coherence is greater for the A3 mooring than for C40 and S1, both of which are $\sim 1R$ from the coast.

At mooring A3, the model underestimates the observed standard deviation by approximately a factor of two (Fig. 13). The reason is not clear, but it could be due to a combination of our approach in evaluating the wind stress, to error in the bottom friction coefficient, and/or to the lack of sea ice, stratification, tides, and a mean Bering Strait throughflow (recall that this model has a near zero net flow, as seen in Fig. 13).

Based on the cross-correlations of low-pass filtered hourly time series, ARVI run #08 has $r^2 = 0.79$ with respect to the observed along-strait A3 current in Bering Strait from October 2008–April 2009, and $r^2 = 0.62$ for May–September 2009. In contrast, the A3 NARR wind record over these intervals have $r^2 = 0.50$ and $r^2 = 0.21$ for the winter and summer observed currents, respectively. Considering the monthly mean velocity anomalies from December 2007 to July 2011, we find that $r^2 = 0.82$ for the model: observed monthly anomalies ($N = 44$, $p = 0$). On a seasonal basis, the relations are $r^2 = 0.87$ for October–April ($N = 26$, $p = 0$) and $r^2 = 0.75$ ($N = 18$, $p = 0$) for May–September. Hence, the ARVI model provides a skillful hindcast of monthly and synoptic-scale current variability and does appreciably better than a regression based purely on reanalysis winds.

The results of ARVI run #08 are next compared for October 2008 through September 2009 to runs in which winds were applied only

south of Bering Strait (run #18), only north of Bering Strait (run #19), and only over the East Siberian Sea (run #20). At site A3 we find that the linear superposition of currents from runs #18 and #19 very closely reproduces the along-principal axis currents from integration #08 ($r^2 = 0.99$, $p = 0$, root mean square difference <1 cm s^{-1}). Current variance and mean and peak currents are shown in Table 3 to provide a context for the relative importance of remotely generated shelf currents, as well as summarizing the statistics of this simple wind-driven homogeneous model, which can be compared to those of the observed currents.

For these one-year integrations, the wind forcing is directly responsible for mean flows of less than 1 cm s^{-1} at C40 and S1 in both summer and winter, only 4 cm s^{-1} at A3 in winter, and up-canyon flows of 4 cm s^{-1} at BC2 in summer and 11 cm s^{-1} at BC2 in winter (Table 3). The near-zero net flow at C40 is consistent with the observations, but not at S1 or A3 (but recall that the ARVI model has no mean Bering Strait transport). Winds over the Bering shelf account for nearly three times the variance at A3 in winter months as do winds north of Bering Strait, but slightly less than twice the variance in summer. We conclude that most of the Bering Strait synoptic scale current and transport variability is generated over the Bering shelf.

The variance in the Bering wind field decreases from winter to summer. In contrast, the East Siberian Sea wind variance is larger in summer than in winter, and as a result the current variance in ARVI integration #20 is greater in summer than in winter (Table 3), even without the potential effects of landfast ice in dissipating shelf wave energy. Thus, ignoring ice effects, East Siberian Sea winds account for $\sim 6\%$ of the Bering Strait variance in winter, but $\sim 12\%$ in summer.

From run #18 we find that Bering Shelf winds account for $\sim 1/3$ of the modeled variance at S1 in the central Chukchi Sea, but $\sim 2/3$ of the variance at BC2, which records the bathymetrically concentrated flow near Barrow Canyon.

As an illustration of the decoupling between northward-propagating shelf waves along the Alaskan Bering Sea coast and southward-propagating waves along the Siberian coast, we computed the variances (s^2) at sites C40 (central Bering shelf), LS1 (Long Strait) and GA1 (Gulf of Anadyr). Model run #18 imparts strong control at C40 and GA1 ($s^2 = 7$ and 25 cm^2 s^{-2}, respectively), but not at LS1 ($s^2 < 0.2$ cm^2 s^{-2}). In contrast, runs #19 and #20 generate s^2 of 17–20 cm^2 s^{-2} at LS1, 2–7 cm^2 s^{-2} at GA1 and <0.3 cm^2 s^{-2} at C40.

As an additional example of the influence of remote forcing on the northeast Chukchi Sea, we use data from an array of six current meter moorings from the head of Barrow Canyon (Weingartner et al., 2013). The moorings, including the BC2 mooring shown in
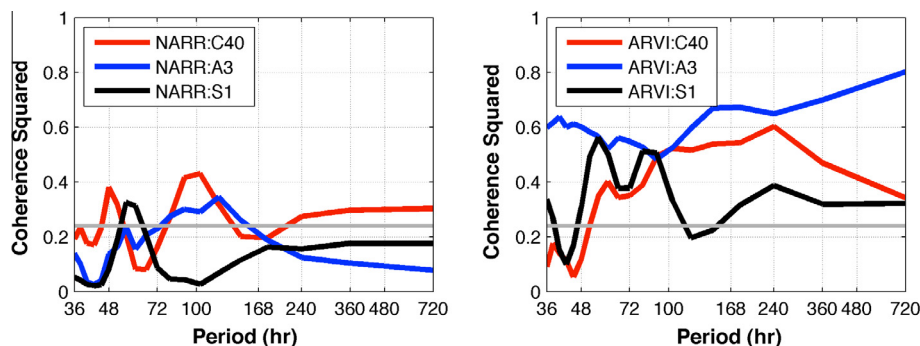
Fig. 12. Coherence-squared between local reanalysis-derived winds and observed currents (left) and the ARVI model hindcast currents and observed currents (right) for October 2008–September 2009. Coherence computations employ a 1-month Hanning window with no overlap; results are smoothed with a 3-point moving average. Following Thompson (1979), with $n = 12$ for one year of month-long windows, gives a 95% significant coherence-squared level of $\gamma^2 = 0.24$ (gray line). Winds and currents used here are shown in Figs. 5 and 10 respectively. Note the improvement in reproducing observed currents by using the vertically integrated model rather than relying solely on local winds.
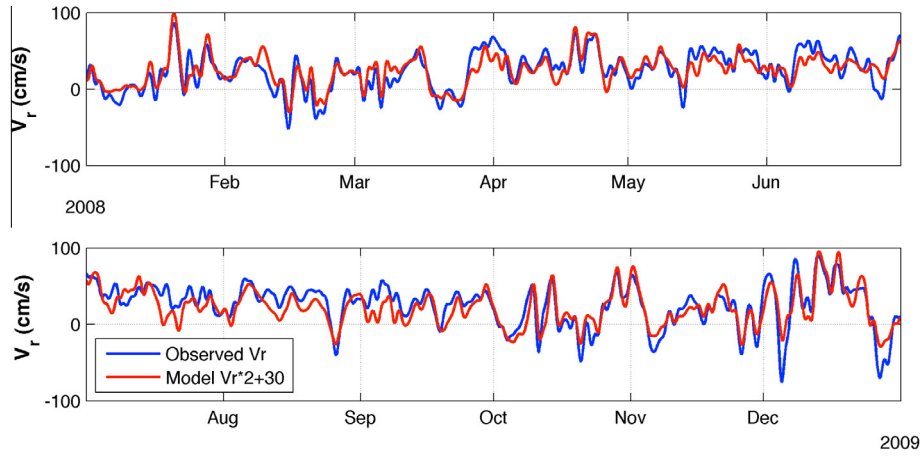
Fig. 13. Observed (blue) and predicted (red) along-axis velocity at monitoring site A3 in 2008. Both records are filtered with a 6th order lowpass Butterworth filter with a 35-h half power cutoff. The vertically integrated model results are scaled by a factor of 2 and offset by 30 cm s^{-1}, the mean difference between the two records.

Table 3
ARVI model variance along the principal axis of variation, mean speed, and maximum speed at sites A3, S1, BC2, C40, LS1, and AG1 for October 2008–April 2009 (winter) and May 2009–September 2009 (summer). Run #08 was forced by winds across the entire ARVI domain; #18, #19 and #20 were forced by winds only south of Bering Strait, north of Bering Strait, and over the East Siberian Sea, respectively.

	Site	Season	Run #08	Run #18	Run #19	Run #20
Variance (cm^2 s^{-2})	A3	W	196.0	115.6	39.4	12.2
	A3	S	121.8	56.7	33.0	14.6
	S1	W	28.3	8.6	17.1	0.4
	S1	S	15.4	4.8	10.3	0.5
	BC2	W	574.9	380.5	298.8	15.2
	BC2	S	419.6	251.0	238.5	18.3
	C40	W	25.3	25.4	0.3	0.2
	C40	S	15.2	15.2	0.3	0.2
	LS1	W	16.6	0.2	16.8	20.3
	LS1	S	18.3	0.1	18.4	20.2
	GA1	W	12.3	11.8	7.4	2.0
	GA1	S	9.7	7.4	7.3	2.6
Mean speed (cm s^{-1})	A3	W	3.8	2.4	1.4	0.4
	A3	S	−0.6	−0.1	−0.6	−0.2
	S1	W	−0.9	0.3	−0.8	0.0
	S1	S	0.0	0.3	0.0	0.1
	BC2	W	−11.5	−6.7	−7.8	0.3
	BC2	S	−4.3	−0.5	−5.1	−0.6
	C40	W	−0.8	−0.8	0.0	0.0
	C40	S	−0.6	−0.6	0.0	0.0
	LS1	W	−1.5	−0.1	1.4	−1.9
	LS1	S	0.3	0.0	0.3	−1.4
	GA1	W	−1.4	−0.6	−0.7	−0.1
	GA1	S	0.1	−0.2	0.5	0.3
Maximum speed (cm s^{-1})	A3	W	42.4	29.1	21.5	13.9
	A3	S	34.6	26.9	18.5	13.1
	S1	W	16.5	10.1	13.7	2.2
	S1	S	16.2	6.5	14.0	2.5
	BC2	W	52.8	39.5	41.3	11.6
	BC2	S	52.4	33.8	42.5	12.4
	C40	W	24.4	24.5	2.3	1.5
	C40	S	16.2	16.2	2.0	1.4
	LS1	W	19.2	1.6	19.1	17.3
	LS1	S	21.2	0.9	21.4	21.0
	GA1	W	13.4	13.5	7.4	3.9
	GA1	S	8.8	7.5	7.0	4.6

Fig. 1, were deployed approximately perpendicular to the Alaskan coast and Barrow Canyon, with the outermost mooring ∼80 km offshore. From these data we create a daily Barrow Canyon transport time series for October 2010–April 2011 (Weingartner et al., 2013). A generalized linear model (GLM) based on NARR winds at sites BC2, A3, and C40 was constructed to determine if remote forcing can account for a significant fraction of the Barrow Canyon

transport. The GLM, a linear multivariate regression of the form $y(t) = A_0 + A_1x_1(t) + A_2x_2(t) + \cdots A_Nx_N(t)$, objectively determines which predictors are included in the final model by selecting the initial and subsequent predictors based on associated *p*-values. Predictors with the smallest *p*-values are selected before predictors with larger *p*-values. Retained terms are those with coefficients that are significantly different from zero at the 95% confidence

level. In this case $N = 6$, with the predictors being the east–west and north–south wind components at the three sites. All six wind coefficients are significant, with winds at BC2 leading the transport response by one day and the remote winds leading the response by two days. The local winds capture the largest fraction (47%) of the October–April transport variance. Using rotated wind components, the following relation accounts for 66% of the observed October–April transport variability at the BC mooring array: $BCT(t) = 0.39 - 0.040V_{C40} + 0.031V_{A3} + 0.096U_{BC2} - 0.046V_{BC2}$, where U_{BC2} is the along-canyon wind at BC2 and V is the daily mean cross-canyon (295°T), along-strait (15°T), and along-shelf (345°T) wind at BC2, A3, and C40, respectively. In summer, the transport variance explained by the regression increases from 12% to 29% when the A3 and C40 winds are included.

In summary, wind stress and the associated Ekman transport, coastal convergences/divergences, and barotropic continental shelf waves together account for a substantial fraction of the synoptic scale current variations in Bering Strait, and on the Bering and Chukchi shelves.

3.4. Variations in the along-strait pressure head

We next return to the topic of multi-year trends in the longitudinal position of the Aleutian Low and their influence on the shelf currents.

Woodgate et al. (2012) found that annual Bering Strait transport anomalies can be as large as 30% of the long-term mean. They also ascribed the observed 2001–2011 transport increase to an increase in the pressure head and a reduction in the opposing wind stress, and concluded that these two mechanisms account for 2/3 and 1/3 of the transport increase, respectively. Aagaard et al. (2006) estimated that variation in the pressure head over 1993–2006 could have been as large as 20% due to thermohaline changes in the Aleutian and Canada basins. Given that the Aleutian Low shifted eastward in 2005 (Fig. 4), but that the observed increase in Bering Strait throughflow extends over a decade centered on this transitional year (Woodgate et al., 2012), we seek evidence for a coincident and altered meridional pressure gradient by comparing the two six-year intervals 2000–2005 and 2006–2011.

Fig. 14 shows SLP maps for these two periods, along with intra-period differences in SLPs, SSH anomalies, and wind stress curl. After the 2005 Aleutian Low eastward shift, SLP increased over the Aleutian Basin and decreased over the Gulf of Alaska (Fig. 14a–c). As a consequence, the mean winter wind orientation over the Bering shelf rotated from the southwest in 2000–2005 toward the south-southwest from 2006–2011 (Fig. 4), while in Bering Strait the mean southward wind stress decreased by ∼20% (see also Fig. 2 of Woodgate et al. (2012)), and the mean westward wind stress nearly doubled (Table 4). In addition, the wind stress curl decreased over the western Bering Sea and Western Subarctic Gyre, while it increased over the Gulf of Alaska and portions of the eastern Bering Sea (Fig. 14f). The Aleutian Basin SSH increased by ∼4–5 cm, while the SSH field decreased slightly over the Gulf of Alaska, the eastern Bering Sea shelf, and much of the Chukchi, Beaufort and East Siberian shelves (Fig. 14e and Table 4), although the SSH map is biased toward ice-free conditions and so must be interpreted with care. The small SSH decrease over the Bering shelf is consistent with the observed shift in wind directions over the shelf, because an eastward-displaced Aleutian Low promotes more upwelling-favorable winds along the western Alaska coast than does a westward-displaced Low. The increased SSH over the Aleutian basin likely results from decreased Ekman divergence within the basin gyre (Gill, 1982; Zhang et al., 2010).

An analogous adjustment occurs in the Beaufort Gyre (Proshutinsky et al., 2002). From 2003–2007, fresh water accumulated in the gyre as SLP and anticyclonic wind stress curl increased

(McPhee et al., 2009; Proshutinsky et al., 2009), resulting in an increase in gyre dynamic height (Proshutinsky et al., 2009; Giles et al., 2012). An increase in anticyclonic wind stress would also promote upwelling along the Arctic coasts, which is consistent with the SSH reduction along the Beaufort, Chukchi and East Siberian Sea coasts during 2006–2011 (Fig. 14e and Table 4). The Canada Basin SSH shows a small increase in mid-gyre during the second period, but this elevation change is both too small and of the wrong direction to account for the observed changes in Bering Strait transport. Figs. 14d reflects an amplified Beaufort High that may be the result of a warming western Arctic troposphere (Moore, 2012) but it is not clear how or whether this warm season signal is linked to the cold season Aleutian Low adjustment shown in Fig. 14c. We note that Serreze and Barrett (2011) show that an enhanced Beaufort High generally corresponds to an enhanced Aleutian Low.

We further consider the observed SSH changes in the Aleutian Basin by examining CTD data, noting that profiles in this region are lacking from 2000 and 2001, but that ARGO float profiles exist after 2001. Because the data coverage is sparse both temporally and spatially, we combine profiles within two different regions for comparison. The first region encompasses the Aleutian and Bowers basins, while the second region is bounded by 50–55°N and 170°E–180°, which aligns closely with the center of the SSH difference maximum in Fig. 14, and contains appreciably more data than from within the Bering Sea basins alone. Although the second region encompasses a portion of the Western Subarctic Gyre south of the Aleutian Islands, SSH changes in this region will add to the large-scale meridional pressure gradient. When referenced to 800 dbar, the dynamic height increased by 0.4 and 0.5 m² s⁻² in the two regions, respectively, from 2002–2005 to 2006–2011. These increases agree well with the altimeter-measured differences of 4 and 5 cm (Table 4), and they are close to the 2001–2006 increase of 5 cm reported by Aagaard et al. (2006). The CTD data show that the dynamic height increase is associated with an average isopycnal lowering of nearly 100 m at 500 m depth, consistent with the observed SSH changes being primarily associated with changes in Ekman divergence in the Western Subarctic Gyre. Although thermohaline processes may also influence the SSH in this region, our conclusion is consistent with the analyses of Lagerloef (1995), Isoguchi et al. (1997) and Zhang et al. (2010), all of whom showed that Ekman pumping is likely the dominant term in setting the SSH variability here.

The decorrelation time scale of SSH anomalies (defined by the time to reach the first zero crossing in the SSH anomaly autocorrelation) is <1 year on the Bering shelf and in the Alaskan Stream but 2–3 years in the Aleutian Basin, consistent with the longer spin-up time required for a baroclinic ocean to adjust to changes in wind stress curl.

We next examine the vertically-integrated momentum balance in Bering Strait along the principal axis of variation for the steady linearized case, where the meridional pressure gradient balances wind and bottom stress:

$$g \frac{dh}{dy} = \frac{\tau^y}{\rho H} - r \frac{V}{H} \qquad (2)$$

If we assume that the previously determined dynamic height gradient between the North Pacific and the Arctic is responsible for the pressure head, then we can solve for the linear friction coefficient, r, using the Pacific–Arctic SSH difference $dh = 0.7$ (Aagaard et al., 2006), the mean observed principal axis velocity $V = 0.25 \text{ m s}^{-1}$ measured at A3, and the mean southward wind stress $\tau^y = -0.027$ Pa at A3, where V and τ^y are the averages for 1997–2011. The endpoint locations are taken to be the southern (Bering) and northern (Chukchi) shelfbreak regions closest to Bering Strait, corresponding to the scale distance (∼2000 km) a
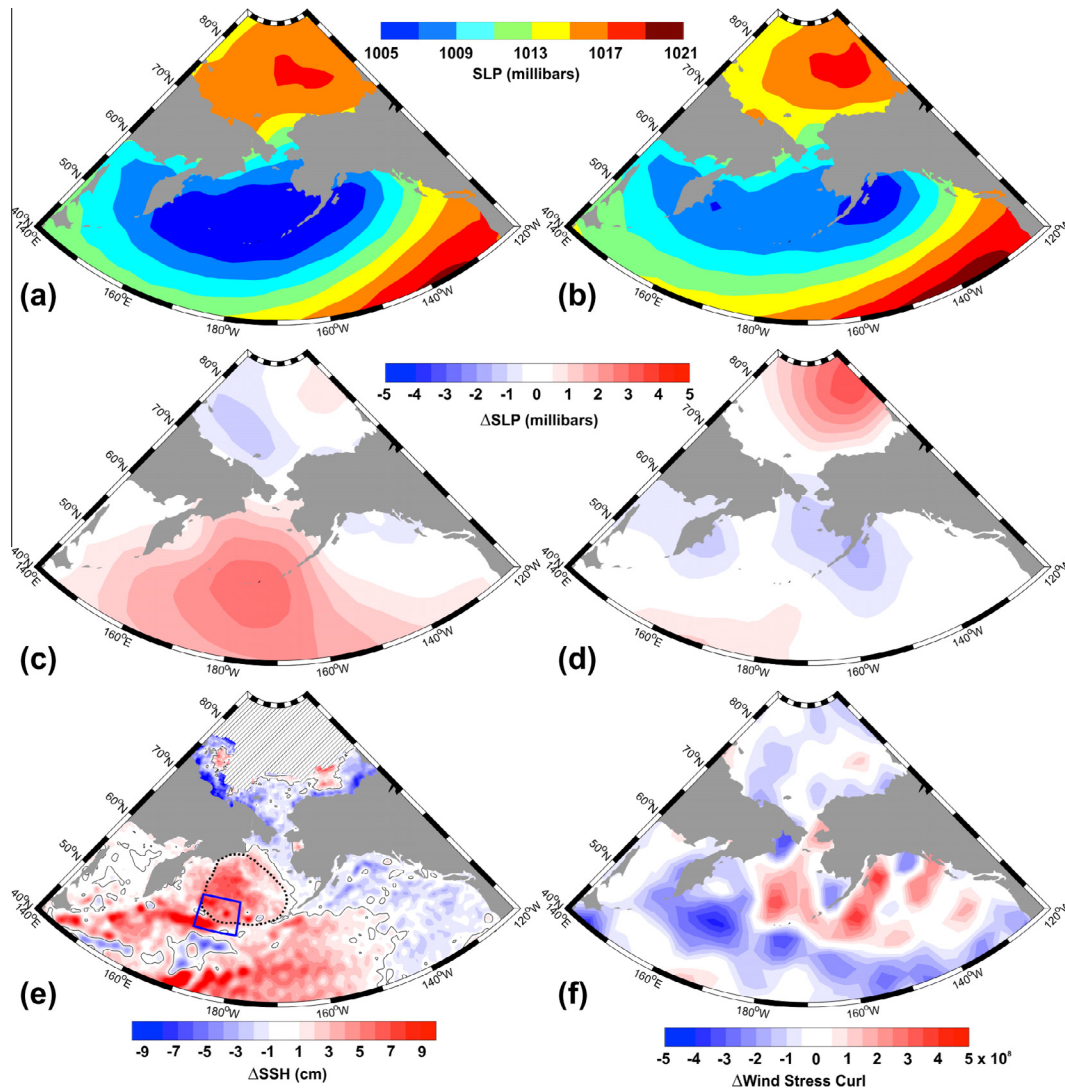
Fig. 14. Top panels show the mean NCEPR SLP averaged over 2000–2005 (a) and 2006–2011 (b). Middle panels show the difference in SLP between these two time intervals for the seasonal subsets of October–April (c) and May–September (d). Bottom panels show the difference between these two time intervals in satellite observations of SSH (e) and the difference in wind stress curl computed from NCEPR (f). In panel (e), sea ice biases some grid cell results to the open water portion of the year and prohibits any computation in the hatched area. The two Aleutian Basin integration regions for SSH anomalies (Table 2) are depicted with the blue box and black dotted line in panel (e).

Table 4
Summary of observed conditions over 2000–2005 (column 2) and 2006–2011 (column three), and of the changes between these two periods (column four) for the parameters listed in column one: the Bering Strait A3 current velocity projected along its principal axis of variation, the V wind stress at A3, the U wind stress at A3, SSH anomalies computed over the three domains listed, and dynamic height (DH) computed from CTD profiles within the two domains listed. The ranges in parentheses in column four represent the 95% confidence limits for the difference between each mean.

	2000–2005	2006–2011	Difference (range)
Bering Strait current V_R (cm s^{-1})	22.6 ± 2.7	27.1 ± 3.0	4.5 (−1.2 to 10.2)
North–South wind stress in Bering Strait (kg m^{-1} s^{-2})	−0.031 ± 0.005	−0.021 ± 0.004	0.01 (0.001 to .019)
East–West wind stress in Bering Strait (kg m^{-1} s^{-2})	−0.008 ± 0.001	−0.017 ± 0.001	−0.009 (0.007 to 0.010)
SSH anomaly Aleutian Basin (cm)	−2.9 ± 0.5	1.3 ± 0.3	4.2 (3.4 to 4.9)
SSH anomaly (cm) for 50°–55°N and 170°E–180°	−3.1 ± 0.4	2.4 ± 0.5	5.4 (4.6 to 6.3)
Southwestern Chukchi Sea SSH anomaly (cm) for 66–70°N and 180°–170°W	1.5 ± 0.4	−1.2 ± 0.5	−2.6 (−3.3 to −1.7)
0–800 m Aleutian Basin dynamic height (m^2 s^{-2})	9.09 ± 0.08	9.47 ± 0.06	0.38 (0.36 to 0.40)
0–800 m 50–55°N and 170°E–180° dynamic height (m^2 s^{-2})	8.96 ± 0.07	9.43 ± 0.04	0.47 (0.36 to 0.58)

typical water parcel flowing over the Bering–Chukchi shelves must take as it flows around the Gulf of Anadyr, through Chrikov Basin, the Bering Strait, across the Hope Valley and then across the Chukchi shelf. For $H = 50$ m, the strait and flow pathway depth, and $dy = 2 \times 10^6$ m, we obtain $r = 6 \times 10^{-4}$ m s^{-1}, consistent with estimates of linear bottom friction coefficients for continental shelves (Brink, 1998; Garvine, 1995).

In the southwestern Chukchi Sea region bounded by 66°N, 70°N, 180° and 170°W, we find valid SSH anomaly estimates in 116 out of the 144 months between 2000 and 2011. The SSH signal is appreciably noisier here than in the Aleutian Basin, but there is a significant (at the 95% confidence level) SSH decrease of 3 cm from the first to the second half of the 2000–2011 time interval (Fig. 14 and Table 4). Upon combining this Chukchi Sea SSH decrease with

the 4–5 cm increase over the Aleutian Basin, the net meridional SSH gradient increased by 7–8 cm, which suggests a 3 cm s^{-1} increase in the Bering Strait mean flow based on Eq. (2). A reduction in opposing wind stress (Table 4) at A3 between the two periods accounts for a 2 cm s^{-1} velocity increase. Together, these values agree well with the observed 4.5 cm s^{-1} increase measured at the moorings Woodgate et al. (2012). We conclude that this combination of local and remote wind forcing can account for the observed Bering Strait velocity increase between these two time intervals, although we cannot preclude additional effects from SSH variations over the Canada Basin, nor possibly of long-term changes in the effects of wind-forced continental shelf waves.

Considering annual averages, the SSH anomaly time series (Fig. 15a) over the Aleutian Basin shows a minimum in 2001 and a maximum in 2011, which agrees with the end points of the Bering Strait transport increase observed by Woodgate et al. (2012). We therefore linearly regress the annually averaged meridional SSH gradient anomaly measured between the Aleutian Basin and the southwest Chukchi Sea (Fig. 15a) against the observed Bering Strait annual velocity anomaly (Fig. 15b) for 1997–2011. The coefficient of variation $r^2 = 0.38$, and the relationship is unaltered if we only consider 1998–2010 (because this time span has year-round data at A3). If we include a separate term for the annually averaged Beaufort Gyre SSH anomaly (not shown) in the GLM regression, we account for 55% of the annual transport anomaly, but note that the regression coefficient associated with the Beaufort Gyre SSH is significant only at the 90% confidence level. Furthermore, the sign of this coefficient is inconsistent with an increase in Bering Strait transport during periods of decreased Beaufort Gyre SSH. Instead, it is consistent with enhanced easterly winds (Table 4) driving coastal divergence (SSH decrease along the north-facing Arctic coast). We conclude that the shelf winds along the Arctic coast and the wind stress curl over the Aleutian Basin and the Western Subarctic Gyre exert primary control over the along-strait pressure gradient.

4. Summary, discussion, and conclusions

4.1. Summary and a conceptual model

Our results suggest that wind forcing on multiple temporal and spatial scales over the North Pacific and western Arctic affects transport through Bering Strait. We summarize our findings in the conceptual diagram shown in Fig. 16. Over the eastern Bering shelf, coastal convergence along western Alaska is favored when the Aleutian Low is centered over the Aleutian Basin (Fig. 16a), giving rise to storm paths that lie considerably farther west than when the Aleutian Low is displaced eastward. The shelf rapidly adjusts to each passing storm, and daily, monthly, and possibly longer averaging periods exhibit SSH anomalies along the Alaskan coast that reflect the influence of surface Ekman transport and coastal convergence, and of shelf waves, all of which contribute to transport variations in Shpanberg, Anadyr, and Bering straits. While shelf waves are not explicitly shown in Fig. 16, they are triggered by the same storms that drive onshore Ekman transport and sea level setup, causing northward velocity anomalies associated with northward propagating waves. As a storm abates, southward velocity anomalies, also associated with northward propagating waves, occur as the sea level re-adjusts. The amplitude of the northward and southward velocity pulses depends upon the magnitude of the wind stress, and probably also on whether the storm system propagates into the Arctic Ocean or onto land, or stalls and dissipates over the Bering Sea.

In addition, a low over the Aleutian Basin enhances cyclonic wind stress curl there, which increases Ekman suction and elevates basin isopycnals. In turn, this leads to a decrease in basin dynamic height, in the along-strait pressure gradient, and in the northward transport through Bering Strait. The opposite responses occur under eastward-displaced storms (Fig. 16b). The oceanic response
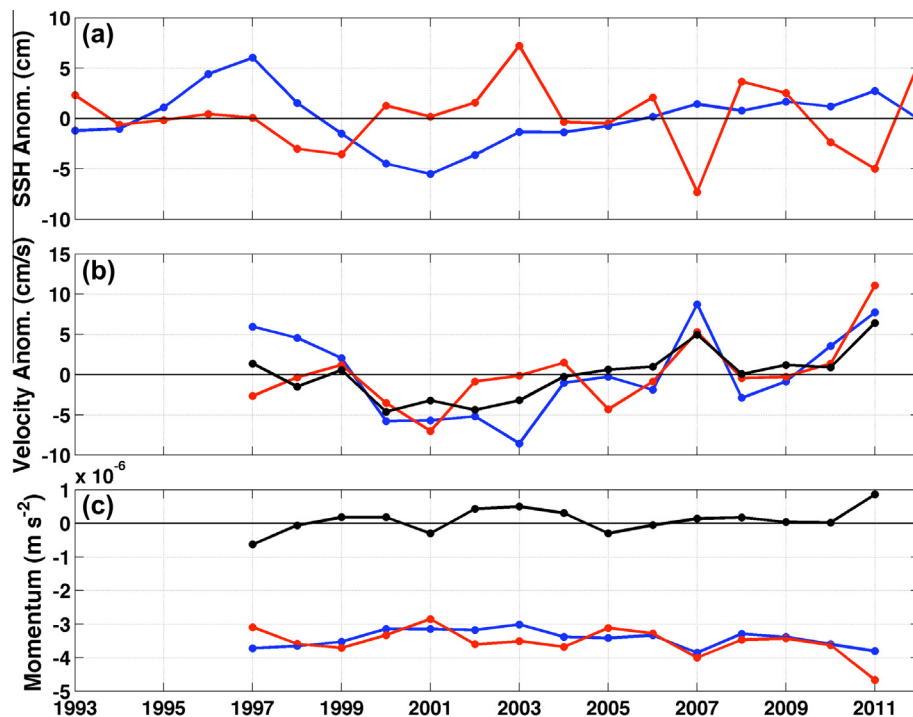
Fig. 15. Panel (a) shows monthly SSH anomalies averaged over the Aleutian Basin (blue) and the southwest Chukchi Sea (red); (b) the observed along-axis A3 annual velocity anomaly (red), against which we regress the meridional SSH gradient anomaly (blue, $r^2 = 0.38$, $p = 0.01$) and both the meridional SSH gradient anomaly and the Beaufort Gyre SSH anomaly (black, $r^2 = 0.55$, $p = 0.01$) and panel c the annual averages of each side of the momentum Eq. (2): the pressure gradient (blue), the wind stress and friction terms (red), and the difference between the two (black). Note that 1997 and 2011 have only about half a year of mooring data each.
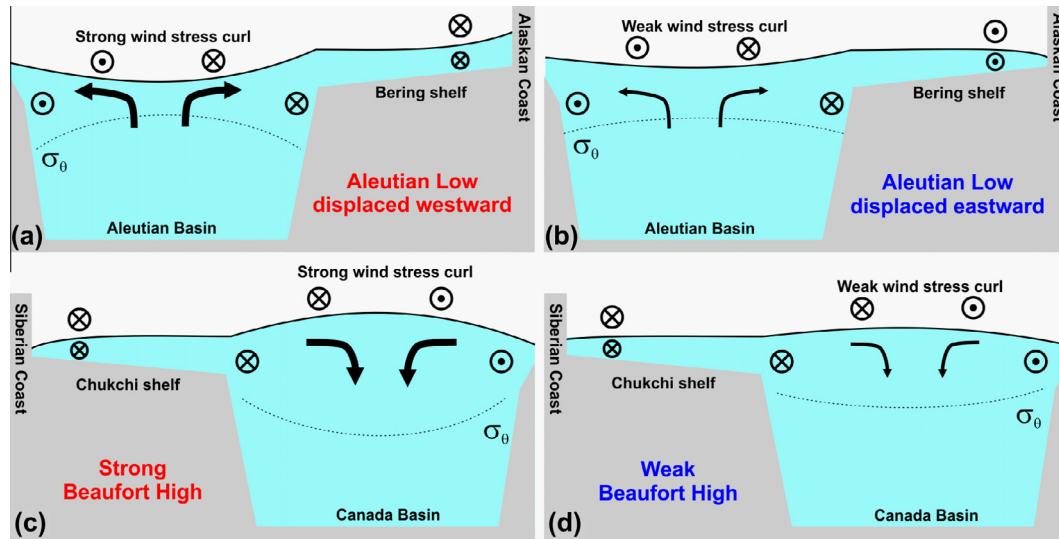
Fig. 16. Conceptual diagrams representing the North Pacific (top) and the western Arctic (bottom) basin-shelf systems. Crosses depict winds and currents flowing into the page and points denote winds and currents directed out of the page. Under a strong Aleutian low centered over the Bering Sea (a), wind stress curl and Ekman suction over the basin increase and the basin dynamic height and SSH decrease, lowering the Pacific–Arctic sea surface height gradient and decreasing the Bering Strait transport (not shown) at inter-annual timescales. Such a westward-displaced low imparts southeasterly wind over the Bering shelf and drives coastal convergence along the western Alaska coastline, resulting in increased northward currents over the eastern shelf and through Bering Strait on synoptic storm timescales. An opposite set of responses (b) occurs when the Aleutian Low shifts eastward into the Gulf of Alaska. In the Arctic, a strong Beaufort High (c) promotes enhanced Ekman pumping and fresh water accumulation in the Canada Basin, which increases the Beaufort Gyre dynamic height and SSH (Proshutinsky et al., 2002), but we do not find a strong causal relation between Canada Basin SSH anomalies and Bering Strait flow anomalies. However, enhanced easterly winds along the southwestern Chukchi coast (also associated with a strong Beaufort High) promote an increase of the Pacific–Arctic pressure head via coastal divergence and thus enhanced Bering Strait throughflow. Via relaxation of coastal divergence (d), Arctic inner shelf SSHs increase with a weaker Beaufort High and subsequently retard the Bering Strait throughflow.

to wind forcing therefore hinges critically on the longitudinal position of the Aleutian Low.

An analogous set of processes is likely at work in the Arctic (Fig. 16c and d), although we discern no Canada Basin influences on the Bering Strait throughflow. Proshutinsky et al. (2002) and others describe a Beaufort Gyre that behaves in a fashion similar to the Aleutian Basin dynamics described here, but we are unable to relate the Beaufort Gyre SSH fluctuations directly to transport variations in Bering Strait. We do, however, identify the direct influence of two related Arctic events on the Bering Strait transport: SSH anomalies in the southwestern Chukchi Sea and shelf waves propagating from the East Siberian Sea and the western Chukchi Sea.

In contrast to the fast (hours and days) response of synoptic scale continental shelf waves, the gyres adjust slowly (years). The decorrelation time scale of SSH anomalies within the Aleutian Basin exceeds two years, and adjustments to steric height are likely mediated by both the mid-gyre upwelling rate and the passage of baroclinic Rossby waves. Over the course of the 2001–2011 Bering Strait transport increase observed by Woodgate et al. (2012), the influence of the remote pressure head changes in the Aleutian Basin appears to have exerted the largest control, although local and regional wind forcing over the shelf also played a significant role.

The dissimilarities in the summer and winter wind-current correlations may be due, at least partially, to coastally trapped waves (Brink, 1998), which are more likely present in the stratified summer season than winter. An assessment of these is beyond the scope of this work.

4.2. Toward improved Bering Strait transport predictability and measurement

A vertically integrated numerical model with 4 km horizontal resolution and a sufficiently broad domain reproduces observed currents with remarkable fidelity, capturing ~80% of the observed Bering Strait subtidal variability during months of strong winds

and weak stratification (October to April) and ~60% in the remainder of the year. The predictive skill of this simple ARVI model could be improved further if forced by wind fields with still better spatial and temporal resolution, but the potential for the largest gains for numerical hindcasts appears to rest in the domain of fully 3-D circulation modeling that resolves buoyancy-driven flows well.

High-resolution numerical model integrations may not be practical for all studies, such as investigations of climate change over a century or more. Univariate regressions based on local winds fail to reproduce the majority of the Bering Strait transport variations, so that their application to climate change and retrospective studies is limited. Regression-based transport estimates may provide sufficient accuracy to improve on the existing regression relations (Coachman and Aagaard, 1981, 1988; Aagaard et al., 1985; Cherniawsky et al., 2005; Woodgate et al., 2012) if remote winds and/or sea surface height anomalies are used in addition to the local winds. In this regard, we find that regressions that include winds over the East Siberian Sea and the central Bering shelf, as well as Bering Strait, appreciably improve predictions of Bering Strait transport variability compared to regressions based on local Bering Strait winds alone.

Satellite altimetry represents a promising tool for remotely monitoring the Bering Strait throughflow on monthly and longer time scales by either estimating the geostrophic flow or the meridional pressure gradient. Advances are underway for improved SSH measurement accuracy in ice covered waters (Giles et al., 2012; Kwok and Morison, 2011), but it will likely be some time before the coverage and quality approach those of ice-free seas.

Maintaining, and possibly supplementing, satellite missions (such as GRACE) and deep CTD and ARGO float measurements in the Aleutian and Canada basins will be critical to future assessments of the role of wind stress curl in Pacific–Arctic exchange.

4.3. Importance to the ecosystem

The monthly and interannual anomalies in Bering Strait velocities observed here and by Woodgate et al. (2005b) and Woodgate

et al. (2012) may play a role in altering the cross-shelf transport of oceanic zooplankton and nutrients. For example, we might expect measurable responses in the Chukchi Sea net primary productivity or net community production (Walsh et al., 1989; Cota et al., 1996; Mathis et al., 2008) when comparing years that fall near either end of the range of observed transports, (e.g., 2001 vs. 2011). Alterations to primary productivity would presumably have a cascading effect on the benthos and marine mammal populations that ultimately depend on the nutrients and organic matter supplied by the Bering Strait throughflow.

We also find appreciable temporal variability in the relative contribution to the Bering Strait throughflow of the transport through Anadyr and Shpanberg straits. Because waters to the east and to the west of St. Lawrence Island carry substantially different nutrient and carbon loads, differential transports of these waters through Bering Strait will influence the regional ecosystem. Likewise, conditions on the central Bering shelf are altered according to whether the onshelf flow through the Gulf of Anadyr is routed northeastward toward Bering Strait or southeastward past St. Lawrence Island. Future changes to the wind fields over the Bering Sea or the western Arctic (Zhang et al., 2004; Salathé, 2006; Sorteberg and Walsh, 2008) could therefore form the basis for significant alterations to cross-shelf pathways and nutrient and plankton fluxes across the Bering shelf and into the Arctic.

5. Conclusions

We have proposed a conceptual model of the Bering–Chukchi circulation as a tightly coupled system responding to multiple modes of forcing that together define the regional flow field. The northward transport through Bering Strait changes on interannual timescales in response to the meridional sea surface elevation gradient, which is set largely over the Aleutian Basin by steric height changes associated with Ekman suction variations within the Western Subarctic Gyre. On synoptic to monthly timescales, current fluctuations on these shelves are primarily due to a combi-

nation of direct local wind stress forcing and remotely forced continental shelf waves. Shelf waves propagate toward Bering Strait from the northwest along the Siberian coastline and from the southeast along the Alaskan coastline. The atmospheric conditions that promote larger Bering Strait transport at annual time scales by increasing the Aleutian Basin steric height also act to reduce Bering Strait transport from the synoptic scale processes. These competing effects combine to determine the net Pacific–Arctic transport.

Appendix A

See Tables A1 and A2

Table A1

Current meter mooring names, locations, dates, and number of samples used in Fig. 2 for measurements between 10 and 20 m depth. Data columns show the mean U and V ocean velocity components under wind $V_R > 0$ and $V_R < 0$ conditions. Boldface type denotes component pairs that are statistically different from each other in the two wind cases. Significance is computed at the 95% confidence level using an ocean current decorrelation time scale of 48 h.

Mooring name or file filename	Latitude	Longitude	Bottom depth	Meas. depth	Start date	End date	#Hours $V_R > 0$	U $V_R > 0$	V $V_R > 0$	#Hours $V_R < 0$	U $V_R < 0$	V $V_R < 0$
N55	−171.97	61.96	54	10	2008/10/1	2010/4/30	3511	0.1	**5.7**	6665	−1.6	**−2.3**
C55	−170.09	60.17	55	10	2008/10/1	2010/4/30	3095	−1.8	**9.2**	5589	−2.4	**−1.3**
S55	−168.39	58.59	55	10	2008/10/1	2010/4/30	3511	−3.4	**5.2**	6665	−3.6	**−1.7**
N40	−169.28	61.81	42	10	2008/10/1	2010/4/30	3511	2.6	**7.2**	6665	−0.5	**−4.0**
C40	−169.02	60.34	41	10	2008/10/1	2010/4/30	3511	−1.4	**8.1**	6665	−1.7	**−5.9**
S40	−167.98	59.14	42	10	2008/10/1	2010/4/30	3511	−1.9	**5.2**	6665	−0.2	**−2.6**
N25	−167.45	61.70	26	10	2008/10/1	2010/4/30	3511	**1.9**	**7.8**	6665	**−2.0**	**−5.6**
C25	−167.34	60.68	26	10	2008/10/1	2010/4/30	3511	**0.8**	**4.5**	6665	**−2.4**	**−3.9**
A1	−169.44	65.90	52	11	2008/10/10	2009/4/20	1898	**14.6**	**45.5**	2995	**−3.2**	**−1.3**
A2W	−168.81	65.80	51	11	2008/10/10	2009/4/20	1902	**3.1**	**53.4**	2995	**−1.9**	4.3
A2	−168.58	65.79	55	11	2008/10/8	2009/4/20	1905	**9.4**	**54.5**	2995	**−0.9**	5.5
A3	−168.96	66.33	57	10	2008/10/7	2009/4/20	1905	**−12.3**	**36.7**	3016	**−4.7**	0.3
A4R	−168.27	65.75	49	10	2008/10/10	2009/4/20	1903	**10.6**	**52.0**	2995	**−0.9**	3.6
H3	−171.59	62.58	48	20	1998/10/1	1999/4/30	2248	−0.4	**3.7**	2840	−0.3	**0.6**
M5	−171.70	59.90	70	14	2008/10/1	2009/4/20	1923	0.1	**4.9**	3165	−2.3	**−1.4**
M8	−174.66	62.20	70	16	2008/10/1	2009/10/1	1923	−0.5	**4.9**	3186	−1.6	**−0.2**
M2	−164.05	56.87	70	13	2007/4/26	2008/4/30	1857	**1.2**	**2.2**	3374	**−2.2**	**−3.2**
an63n165b79ax_018	−165.41	63.48	21	18	1979/11/9	1980/4/30	1728	2.8	6.6	2562	4.5	2.1
NC17	−167.06	62.88	30	18	1981/11/1	1982/4/1	1783	**5.7**	**17.3**	1916	**−2.4**	**−4.8**
an63n171a84ax_015	−171.45	63.28	35	15	1984/10/4	1985/4/30	2419	**−11.9**	−2.2	2590	**20.2**	−5.0
an63n171a84ax_018	−170.56	63.24	25	18	1984/10/4	1985/4/30	2419	**1.3**	0.7	2595	**5.2**	−0.6
an63n171a84ax_020	−170.61	63.15	38	20	1984/10/4	1985/4/30	2419	−3.2	0.0	2594	1.8	−2.5
BS4	−168.87	57.85	66	15	2000/10/1	2001/4/30	2865	**1.0**	−0.4	2223	**−1.8**	−1.0
BS2	−168.55	58.64	57	15	1998/10/2	1999/4/24	2148	**0.8**	2.8	2746	**−2.6**	0.5
nb59n172a82ax_012	−171.66	58.62	104	12	1982/10/22	1983/4/22	1950	−1.4	**7.2**	2615	−4.7	**2.1**
nb59n172a82ax_014	−171.58	59.26	79	14	1982/10/23	1983/4/22	1950	−1.0	**5.9**	2601	−4.7	**0.4**
nb59n173a82ax_012	−172.76	58.53	109	12	1982/10/22	1983/4/22	1950	**−0.6**	7.2	2624	**−5.6**	3.2
SP2	−170.33	57.13	12	16	1995/10/1	1996/4/30	2434	**4.0**	**−3.1**	2678	**6.2**	**−0.4**
SP4	−170.43	57.15	29	19	1995/10/1	1996/4/30	2434	**−17.9**	**7.8**	2678	**−15.4**	**3.9**

Table A2

Current meter mooring names, locations, dates, and number of samples used in Fig. 2 for measurements between 30 and 60 m depth. Data columns show the mean U and V ocean velocity components under wind $V_R > 0$ and $V_R < 0$ conditions. Boldface type denotes component pairs that are statistically different from each other in the two wind cases. Significance is computed at the 95% confidence level using an ocean current decorrelation time scale of 48 h.

Mooring name or filename	Latitude	Longitude	Bottom depth	Meas. depth	Start date	End date	#Hours $V_R > 0$	U $V_R > 0$	V $V_R > 0$	#Hours $V_R < 0$	U $V_R < 0$	V $V_R < 0$
N55	−171.97	61.96	54	30	2008/10/1	2010/4/30	3511	0.0	**3.6**	6665	−0.4	**−1.7**
an61n171a81ax_037	−170.60	60.57	56	37	1981/10/31	1982/4/30	1997	0.2	3.5	5589	1.4	−0.6
an59n172a82ax_039	−171.66	58.62	104	39	1982/10/22	1983/4/22	1950	−2.1	3.4	6665	−2.1	1.8
an59n173a82ax_045	−172.76	58.53	109	45	1982/10/22	1983/4/22	1950	−2.0	5.5	6665	−3.2	2.2
an59n172a82ax_036	−171.58	59.26	79	36	1982/10/23	1983/4/22	1950	−2.6	3.1	6665	−1.7	0.8
an60n171a82ax_045	−170.68	59.83	61	45	1982/10/23	1983/4/22	1950	−2.6	4.4	6665	−1.5	0.8
an60n169a84ax_035	−169.27	60.09	44	35	1984/10/3	1985/4/30	2419	0.5	**9.4**	3159	0.3	**−1.7**
BP3	−169.27	56.12	872	52	1989/10/1	1990/4/30	2073	−5.3	0.3	3262	−6.1	1.2
BS3	−173.29	56.67	878	45	1989/10/1	1990/10/3	2109	−14.8	13.5	3262	−11.9	9.3
MA1	−169.43	65.90	50	41	1990/10/1	1991/4/30	2111	**14.1**	**30.5**	3262	**3.2**	**2.7**
MA2	−168.59	65.78	53	44	1990/10/1	1991/4/30	2111	1.9	**37.4**	3262	3.5	**6.4**
MA3	−168.97	66.29	56	47	1990/10/1	1991/4/30	2111	−10.0	**28.9**	3262	**0.7**	**5.1**
MC1	−174.55	67.95	44	35	1990/10/1	1991/10/4	2160	0.0	0.9	3262	1.3	0.6
MC2	−172.50	68.34	51	42	1990/10/1	1991/4/30	2111	−3.7	4.3	2977	0.3	2.2
MC3	−171.07	68.61	55	47	1990/10/1	1991/4/30	2111	−5.1	**7.3**	2977	−1.0	**1.3**
MC4	−169.59	68.86	53	44	1990/10/1	1991/4/30	2111	−3.4	**9.0**	2977	−2.0	**0.6**
MC6	−166.96	69.02	47	38	1990/10/1	1991/4/30	2111	0.4	**9.0**	3018	0.1	**−0.4**
ME2	−181.55	70.50	46	37	1990/10/1	1991/4/30	2111	−3.5	0.5	2977	−3.1	1.4
MF1	−175.73	71.12	48	39	1990/10/1	1991/1/14	1102	−0.1	0.8	2977	0.2	0.5
MF2	−174.19	70.96	49	40	1990/10/1	1991/4/30	2111	0.5	9.9	2977	−0.4	9.2
AC2	−163.29	70.75	46	42	1994/10/1	1995/4/21	1826	**8.1**	4.8	2977	**2.0**	1.7
C1	−167.08	70.62	55	49	1994/10/1	1995/4/21	1826	0.7	**12.2**	2977	−0.5	**4.0**
C2	−164.45	71.33	46	42	1994/10/1	1995/4/21	1826	**6.7**	1.1	1424	**1.8**	−1.4
C3	−167.19	71.68	49	43	1994/10/1	1995/4/21	1826	3.3	**5.6**	2977	1.2	**2.3**
EBC	−157.62	71.35	107	52	1994/10/1	1995/4/21	1826	16.8	4.7	2840	1.5	1.7
PBC	−157.52	71.25	63	57	1994/10/1	1995/4/21	1826	11.4	8.9	2840	5.6	4.3
AC1	−166.23	69.99	46	42	1994/10/6	1995/4/21	1791	3.9	4.2	2840	1.7	1.5
SP1	−170.15	57.02	69	55	1995/10/1	1996/4/30	2434	−2.1	0.2	2840	−3.8	−0.5
UP4	−164.73	54.37	59	46	1996/10/1	1997/4/30	1918	−29.1	−5.0	2840	−22.4	−6.2
H1	−172.17	63.16	60	55	1998/10/1	1999/4/30	2248	−2.4	4.4	3165	3.6	2.0
H3	−171.59	62.58	48	43	1998/10/1	1999/4/30	2248	0.1	**4.0**	3186	0.1	**0.0**
H4	−170.83	62.44	42	37	1998/10/1	1999/4/30	2248	0.2	4.1	3374	−0.5	0.6
H5	−170.00	62.67	42	37	1998/10/1	1999/4/30	2248	**7.8**	**5.5**	2601	**1.9**	**2.2**
F4	−170.55	62.92	44	40	1998/10/1	1999/4/30	2248	5.9	−2.5	2614	1.3	−1.1
M2	−164.05	56.87	70	45	2007/4/26	2008/4/30	1857	0.3	1.1	2628	−1.1	0.2
C55	−170.09	60.17	55	30	2008/10/1	2010/4/30	3095	−1.2	**6.4**	2618	0.4	**−1.1**
S55	−168.39	58.59	55	30	2008/10/1	2010/4/30	3511	−2.7	**3.4**	2595	−1.5	**−0.2**
N40	−169.28	61.81	42	30	2008/10/1	2010/4/30	3511	1.5	**4.7**	2369	1.2	**−3.2**
C40	−169.02	60.34	41	30	2008/10/1	2010/4/30	3511	−1.6	**5.5**	3015	0.3	**−4.5**
S40	−167.98	59.14	42	30	2008/10/1	2010/4/30	3511	**−1.8**	**3.6**	2678	**1.2**	**−0.5**
M5	−171.70	59.90	70	38	2008/10/1	2009/4/20	1923	0.7	**3.0**	3070	0.2	**−0.1**
M8	−174.66	62.20	70	44	2008/10/1	2009/10/1	1923	−0.2	4.6	3170	−0.7	1.0

References

Aagaard, K., Carmack, E.C., 1989. The role of sea–ice and other fresh water in the Arctic Circulation. Journal of Geophysical Research: Oceans 94, 14485–14498. http://dx.doi.org/10.1029/89JC01375.

Aagaard, K., Coachman, L.K., Carmack, E.C., 1981. On the halocline of the Arctic Ocean. Deep Sea Research Part A 28, 529–545.

Aagaard, K., Roach, A.T., Schumacher, J.D., 1985. On the wind-driven variability of the flow through Bering Strait. Journal of Geophysical Research: Oceans 90, 7213–7221.

Aagaard, K., Weingartner, T.J., Danielson, S.L., Woodgate, R.A., Johnson, G.C., Whitledge, T.E., 2006. Some controls on flow and salinity in Bering Strait. Geophysical Research Letters 33, L19602. http://dx.doi.org/10.1029/2006GL026612.

Allen, J.S., 1976. Continental Shelf waves and alongshore variations in bottom topography and coastline. Journal of Physical Oceanography 6, 864–878.

Bloom, G.L., 1964. Water transport and temperature measurements in the eastern Bering Strait 1953–1958. Journal of Geophysical Research 69, 3335–3354.

Boyer, T.P., Antonov, J.I., Baranova, O.K., Garcia, H.E., Johnson, D.R., Locarnini, R.A., Mishonov, A.V., O'Brien, T.D., Seidov, D., Smolyar, I.V., Zweng, M.M., 2009. World Ocean Database, 2009. In: Levitus, S. (Ed.), NOAA Atlas NESDIS 66, U.S. Gov. Printing Office, Wash., DC.

Brink, K.H., 1998. Wind-driven currents over the continental shelf. The Sea 10, 3–20.

Budgell, W.P., 2005. Numerical simulation of ice-ocean variability in the Barents Sea region: towards dynamical downscaling. Ocean Dynamics 55, 370–387. http://dx.doi.org/10.1007/s10236-005-0008-3.

Carton, J.A., Chepurin, G., Cao, X., Giese, B.S., 2000a. A Simple Ocean Data Assimilation analysis of the global upper ocean 1950–1995, Part 1: methodology. J. Phys. Oceanogr. 30, 294–309.

Carton, J.A., Chepurin, G., Cao, X., 2000b. A Simple Ocean Data Assimilation analysis of the global upper ocean 1950–1995 Part 2: results. J. Phys. Oceanogr. 30, 311–326.

Carton, J.A., Giese, B.S., 2008. A reanalysis of ocean climate using simple ocean data assimilation (SODA). Monthly Weather Review 136, 2999–3017. http://dx.doi.org/10.1175/2007MWR1978.1.

Chapman, D.C., 1985. Numerical treatment of cross-shelf open boundaries in a barotropic coastal ocean model. Journal of Physical Oceanography 15, 1060–1075.

Cherniawsky, J.Y., Crawford, W.R., Nikitin, O.P., Carmack, E.C., 2005. Bering Strait transports from satellite altimetry. Journal of Marine Research 63 (5), 887–900.

Clement, J.L., Maslowski, W., Cooper, L., Grebmeier, J., Walczowski, W., 2005. Ocean circulation and exchanges through the northern Bering Sea—1979–2001 model results. Deep-Sea Research II. 52, 3509–3540.

Coachman, L.K., Aagaard, K., 1966. On the water exchange through Bering Strait. Limnology Oceanography 11 (1), 44–59.

CNES, 2013. Ssalto/Duacs User Handbook: (M)SLA and (M)ADT Near-Real Time and Delayed Time Products. Aviso, CLS-DOS-NT-06-034, Issue 3.4.

Coachman, L.K., Aagaard, K., 1981. Re-evaluation of water transports in the vicinity of Bering Strait. In: Hood, D.W., Calder, J.A. (Eds.), The Eastern Bering Sea Shelf: Oceanography and Resources, vol. 1. National Oceanic and Atmospheric Administration, Washington, DC, pp. 95–110.

Coachman, L.K., Aagaard, K., 1988. Transports through Bering Strait: annual and interannual variability. Journal of Geophysical Research: Oceans 93 (C12), 15535–15539.

Coachman, L.K., Aagaard, K., Tripp, R.B., 1975. Bering Strait: The Regional Physical Oceanography. Univ. of Wash. Press, Seattle, WA.

Coachman, L.K., 1993. On the flow field in the Chirikov Basin. Continental Shelf Research 13, 481–508.

Cota, G.F., Pomeroy, L.R., Harrison, W.G., Jones, E.P., Peters, F., Sheldon, W.M., Weingartner, T.R., 1996. Nutrients, primary production and microbial heterotrophy in the southeastern Chukchi Sea: Arctic summer nutrient depletion and heterotrophy. Marine Ecology Progress Series 135, 247–258.

Curchitser, E.N., Haidvogel, D.B., Hermann, A.J., Dobbins, E.L., Powell, T.M., Kaplan, A., 2005. Multi-scale modeling of the North Pacific Ocean: assessment and analysis of simulated basin-scale variability (1996–2003). Journal of Geophysical Research: Oceans 110, C11021. http://dx.doi.org/10.1029/2005JC002902.

Cushman-Roisin, B., 1994. Introduction to Geophysical Fluid Dynamics. Prentice Hall, Upper Saddle River, N. J., p. 320.

Dai, A., Qian, T., Trenberth, K.E., Milliman, J.D., 2009. Changes in continental freshwater discharge from 1948–2004. Journal of Climate 22, 2773–2791.

Danielson, S., Aagaard, K., Weingartner, T., Martin, S., Winsor, P., Gawarkiewicz, G., Quadfasel, D., 2006. The St. Lawrence polynya and the Bering shelf circulation: new observations that test the models. Journal of Geophysical Research: Oceans J111, C09023. http://dx.doi.org/10.1029/2005JC003268.

Danielson, S., Eisner, L., Weingartner, T., Aagaard, K., 2011a. Thermal and haline variability over the central Bering Sea shelf: seasonal and inter-annual perspectives. Continental Shelf Research. http://dx.doi.org/10.1016/j.csr.2010.12.010.

Danielson, S., Curchitser, E., Hedstrom, K., Weingartner, T., Stabeno, P., 2011b. On ocean and sea ice modes of variability in the Bering Sea. Journal of Geophysical Research: Oceans 116, C12034. http://dx.doi.org/10.1029/2011JC007389.

Danielson, S., Hedstrom, K., Aagaard, K., Weingartner, T., Curchitser, E., 2012a. Wind-induced reorganization of the Bering shelf circulation. Geophysical Research Letters 39, L08601. http://dx.doi.org/10.1029/2012GL051231.

Danielson, S., Weingartner, T., Aagaard, K., Zhang, J., Woodgate, R., 2012b. Circulation on the central Bering Sea shelf, July 2008 to July 2010. Journal of Geophysical Research: Oceans 117, C10003. http://dx.doi.org/10.1029/2012JC008303.

De Boer, A.M., Nof, D., 2004a. The exhaust valve of the North Atlantic. Letter in Journal of Climate 17, 417–422.

De Boer, A.M., Nof, D., 2004b. The Bering Strait's grip on the Northern Hemisphere Climate. Deep Sea Research Part I 51, 1347–1366.

Emery, W.J., Thomson, R.E., 2001. Data Analysis Methods in Physical Oceanography. Elsevier, xvi + 638pp.

Fedorova, Z.P., Yankina, Z.S., 1963. Supply of Pacific Ocean water through Bering Strait into Chukchi Sea. Okeanologiya 3, 777–784 (in Russian).

Flather, R.A., 1976. A tidal model of the northwest European continental shelf. Memoires de la Societe Royale de Sciences de Liege 6, 141–164.

Garvine, R.W., 1995. A dynamical system of classifying buoyant coastal discharges. Continental Shelf Research 15, 1585–1596.

Gawarkiewicz, G., Haney, J.C., Caruso, M.J., 1994. Summertime synoptic variability of frontal systems in the northern Bering Sea. Journal of Geophysical Research: Oceans 99, 7617–7625. http://dx.doi.org/10.1029/94JC00259.

Giles, K.A., Laxon, S.W. Ridout, A.L., Wingham, D.J., Bacon, S., 2012. Western Arctic Ocean freshwater storage increased by wind- driven spin-up of the Beaufort Gyre. Nature Geoscience. http://dx.doi.org/10.1038/ngeo1379.

Gill, A.E., 1982. Atmosphere–Ocean Dynamics. Academic, San Diego, Calif., 662pp.

Goosse, H., Campin, J.M., Fichefet, T., Deleersnijder, E., 1997. Sensitivity of a global ice–ocean model to the Bering Strait throughflow. Climate Dynamics 13 (5), 349–358.

Grebmeier, J.M., Mcroy, C.P., Feder, H.M., 1988. Pelagic-benthic coupling on the shelf of the northern Bering and Chukchi Seas I. Food supply source and benthic biomass. Marine Ecology Progress Series 48, 57–67.

Hu, A., Meehl, G.A., Otto-Bliesner, B.L., Waelbroeck, C., Han, W., Loutre, M.-F., Lambeck, K., Mitrovica, J.X., Rosenbloom, N., 2010. Influence of Bering Strait flow and North Atlantic circulation on glacial sea level changes. Nature Geoscience 3, 118–121. http://dx.doi.org/10.1038/ngeo729.

Hunke, E.C., Dukowicz, J.K., 1997. An elastic-viscous-plastic model for sea ice dynamics. Journal of Physical Oceanography 27, 1849–1867. http://dx.doi.org/10.1175/ 1520-0485(1997) 027<1849:AEVPMF>2.0.CO;2.

Hunke, E.C., 2001. Viscous-plastic sea ice dynamics with the EVP model: linearization issues. Journal of Computational Physics 170, 18–38. http://dx.doi.org/10.1006/jcph.2001.6710.

Isoguchi, O., Kawamura, H., Kono, T., 1997. A study on wind-driven circulation in the subarctic North Pacific using TOPEX/POSEIDON alti-meter data. Journal of Geophysical Research: Oceans 102 (C6), 12457–12468.

Jakobsson, M. et al., 2012. The International Bathymetric Chart of the Arctic Ocean (IBCAO) Version 3.0. Geophysical Research Letters 39, L12609. http://dx.doi.org/10.1029/2012GL052219.

Johnson, W., Kowalik, Z., 1986. Modeling of storm surges in the Bering Sea and Norton Sound. Journal of Geophysical Research: Oceans 91 (C4), 5119–5128.

Kalnay, E., Kanamitsu, M., Kistler, R., Collins, W., Deaven, D., Gandin, L., Iredell, M., Saha, S., White, G., Woollen, J., Zhu, Y., Leetmaa, A., Reynolds, R., Chelliah, M., Ebisuzaki, W., Higgins, W., Janowiak, J., Mo, K.C., Ropelewski, C., Wang, J., Jenne, R., Joseph, D., 1996. The NCEP/NCAR 40-year reanalysis project. Bulletin of the American Meteorological Society 77, 437–470.

Kasper, J.L., Weingartner, T.J., 2012. Modeling winter circulation under landfast ice. The interaction of winds with landfast ice. Journal of Geophysical Research: Oceans 117 (C04006), 14. http://dx.doi.org/10.1029/2011JC007649.

Kinder, T.H., Schumacher, J.D., 1981. Circulation over the continental shelf of the Southeastern Bering Sea. In: Hood, D.W., Calder, J.A. (Eds.), The Eastern Bering Sea Shelf, Oceanography and Resources, vol. 1. Univ. of Wash, Press, Seattle, WA, pp. 53–75.

Kinder, T.J., Chapman, D.C., Whitehead, J.A., 1986. Westward intensification of the mean circulation on the Bering Sea shelf. Journal of Physical Oceanography 16, 1217–1229.

Kwok, R., Morison, J., 2011. Dynamic topography of the ice-covered Arctic Ocean from ICESAT. Geophysical Research Letters 38, L02501.

Lagerloef, G.S.E., 1995. Interdecadal variations in the Alaska gyre. Journal of Physical Oceanography 25, 2242–2258.

Large, W.G., Pond, S., 1981. Open ocean momentum flux measurements in moderate to strong winds. Journal of Physical Oceanography 11, 324–336. http://dx.doi.org/10.1175/1520-0485(1981) 011<0324:OOMFMi>2.0.CO;2.

Large, W.G., Yeager, S.G., 2009. The global climatology of an interannually varying air-sea flux data set. Climate Dynamics 33, 341–364. http://dx.doi.org/10.1007/s00382-008-0441-3.

Le Traon, P.Y., Dibarboure, G., 1999. Mesoscale mapping capabilities of multi-satellite altimeter missions. Journal of Atmospheric and Oceanic Technology 16, 1208–1223.

Mathis, J.T., Bates, N.R., Hansell, D.A., Babila, T., 2008. Interannual variability of net community production over the Northeast Chukchi Sea Shelf. Deep Sea Research II. http://dx.doi.org/10.1016/j.dsr2.2008.10.017.

McPhee, M.G., Proshutinsky, A., Morison, J.H., Steele, M., Alkire, M.B., 2009. Rapid change in freshwater content of the Arctic Ocean. Geophysical Research Letters 36, L10602.

Mellor, G.L., Kantha, L., 1989. An ice–ocean coupled model. Journal of Geophysical Research 94, 10937–10954. http://dx.doi.org/10.1029/JC094iC08p10937.

Mesinger, F., DiMego, G., Kalnay, E., Mitchell, K., Shafran, P.C., Ebisuzaki, W., Jović, D., Woollen, J., Rogers, E., Berbery, E.H., Ek, M.B., Fan, Y., Grumbine, R., Higgins, W., Li, H., Lin, Y., Manikin, G., Parrish, D., Shi, W., 2006. North American regional re-analysis. Bulletin of the American Meteorological Society 87, 343–360. http://dx.doi.org/10.1175/BAMS-87-3-343.

Moore, G.W.K., 2012. Decadal variability and a recent amplification of the summer Beaufort Sea High. Geophysical Research Letters 39, L10807. http://dx.doi.org/10.1029/2012GL051570.

Mountain, D.G., Coachman, L.K., Aagaard, K., 1976. On the flow through Barrow Canyon. Journal of Physical Oceanography 6, 461–470.

Muench, R.D., Schumacher, J.D., Salo, S.A., 1988. Winter currents and hydrographic conditions on the northern central Bering Sea shelf. Journal of Geophysical Research: Oceans 93 (C1), 516–526. http://dx.doi.org/10.1029/JC093iC01p00516.

Overland, J.E., Roach, A.T., 1987. Northward flow in the Bering and Chukchi seas. Journal of Geophysical Research: Oceans 92, 7097–7105.

Overland, J.E., Adams, J.M., Bond, N.A., 1999. Decadal variability of the Aleutian Low and its relation to high-latitude circulation. Journal of Climate 12, 1542–1548. http://dx.doi.org/10.1175/1520-0442(1999) 012<1542:DVOTAL>2.0.CO;2.

Overland, J.E., Wang, M., Wood, K.R., Percival, D.B., Bond, N.A., 2012. Recent Bering Sea warm and cold events in a 95-year context. Deep Sea Research II 65–70, 6–13. http://dx.doi.org/10.1016/j.dsr2.2012.02.013. ISSN:0967-0645.

Pickart, R.S., Moore, G.W.K., Macdonald, A.M., Renfrew, I.A., Walsh, J.E., Kessler, W.S., 2009. Seasonal evolution of Aleutian low-pressure systems: Implications for North Pacific sub-polar circulation. Journal of Physical Oceanography 39, 1317–1339.

Proshutinsky, A.Y., Johnson, M.A., 1997. Two circulation regimes of the wind-driven Arctic Ocean. Journal of Geophysical Research: Oceans 102, 12493–12514. http://dx.doi.org/10.1029/97JC00738.

Proshutinsky, A., Bourke, R.H., McLaughlin, F.A., 2002. The role of the Beaufort Gyre in Arctic climate variability: seasonal to decadal climate scales. Geophysical Research Letters 29, 2100. http://dx.doi.org/10.1029/2002GL015847.

Proshutinsky, A., Krishfield, R., Timmermans, M.-L., Toole, J., Carmack, E., McLaughlin, F., Williams, W.J., Zimmermann, S., Itoh, M., Shimada, K., 2009. The Beaufort Gyre Fresh Water Reservoir: state and variability from observations. Journal of Geophysical Research: Oceans 114. http://dx.doi.org/10.1029/2008 JC005104.

Ratmanov, G.E., 1937. On the question of water exchange through Bering Strait. Issledovaniya Morei SSSR 25, 119–135 (in Russian).

Reed, R.J., Kunkel, B.A., 1960. The arctic circulation in summer. Journal of Meteorology 17, 489–506.

Rienecker, M., Suarez, M., Gelaro, R., Todling, R., Bacmeister, J., Liu, E., Bosilovich, M., Schubert, S., Takacs, L., Kim, G., Bloom, S., Chen, J., Collins, D., Conaty, A., Da Silva, A., Gu, W., Joiner, J., Koster, R., Lucchesi, R., Molod, A., Owens, T., Pawson, A., Pegion, P., Redder, C., Reichle, R., Robertson, F., Ruddick, A., Sienkiewicz, M., Woollen, J., 2011. MERRA: NASA's modern-era retrospective analysis for research and applications. Journal of Climate 24, 3624–3648. http://dx.doi.org/10.1175/JCLI-D-11-00015.1.

Roach, A.T., Aagaard, K., Pease, C.H., Salo, S.A., Weingartner, T., Pavlov, V., Kulakov, M., 1995. Direct measurements of transport and water properties through Bering Strait. Journal of Geophysical Research: Oceans 100, 18443–18457.

Røed, L.P., Debernard, J., 2004. Description of an Integrated Flux and Sea–Ice Model Suitable for Coupling to an Ocean an Atmosphere Model, Rep. 4, Norw. Meteorol. Inst., Oslo, 51pp.

Salathé Jr., E.P., 2006. Influences of a shift in North Pacific storm tracks on western North American precipitation under global warming. Geophysical Research Letters 33, L19820. http://dx.doi.org/10.1029/2006GL026882.

Sambrotto, R.N., Goering, J.J., McRoy, C.P., 1984. Large yearly production of phytoplankton in the western Bering Strait. Science 225, 1147–1150.

Schlitzer, R., 2002. Interactive analysis and visualization of geoscience data with Ocean Data View. Computers & Geosciences 28, 10, 1211–1218. http://dx.doi.org/10.1016/S0098-3004(02)00040-7. ISSN:0098-3004.

Schumacher, J.D., Kinder, T.H., 1983. Low-frequency current regimes over the Bering Sea Shelf. Journal of Physical Oceanography 13, 607–623.

Schumacher, J., Aagaard, K., Pease, C., Tripp, R., 1983. Effects of a shelf polynya on flow and water properties in the Northern Bering Sea. Journal of Geophysical Research: Oceans 88 (C5), 2723–2732.

Serreze, M.C., Barrett, A.P., 2011. Characteristics of the Beaufort Sea High. Journal of Climate 24, 159–182. http://dx.doi.org/10.1175/2010JCLI3636.1.

Serreze, M.C., Box, J.E., Barry, R.G., Walsh, J.E., 1993. Characteristics of Arctic synoptic activity, 1952–1989. Meteorology and Atmospheric Physics 51, 147–164.

Serreze, M.C., Barrett, A.P., Slater, A.G., Woodgate, R.A., Aagaard, K., Lammers, R.B., Steele, M., Moritz, R., Meredith, M., Lee, C.M., 2006. The large-scale freshwater cycle of the Arctic. Journal of Geophysical Research: Oceans 111, C11010. http://dx.doi.org/10.1029/2005JC003424.

Shaffer, G., Bendtsen, J., 1994. Role of the Being Strait in controlling North Atlantic Ocean circulation and climate. Nature 367, 354–357. http://dx.doi.org/10.1038/367354a0.

Shimada, K., Kamoshida, T., Itoh, M., Nishino, S., Carmack, E., McLaughlin, F., Zimmermann, S., Proshutinsky, A., 2006. Pacific Ocean inflow: influence on catastrophic reduction of sea ice cover in the Arctic Ocean. Geophysical Research Letters 33, L08605. http://dx.doi.org/10.1029/2005GL025624.

Shtokman, V.B., 1957. Vliyanie vetra na techeniya v Beringovo Prolive, prichiny ikh bol'shikh skorostei i preobladayuesheeho severnogo napravleniya, Trans. Inst. Okeanolog., Akad. Nauk SSSR 25, 171–197 (Translated by L.K. Coachman).

Sorteberg, A., Walsh, J.E., 2008. Seasonal cyclone variability at 70°N and its impact on moisture transport into the Arctic. Tellus Series A 60, 570–586. http://dx.doi.org/10.1111/j.1600-0870.2008.00314.x.

Spall, M.A., 2007. Circulation and water mass transformation in a model of the Chukchi Sea. Journal of Geophysical Research: Oceans 112, C05025. http://dx.doi.org/10.1029/2005JC003364.

Springer, A.M., McRoy, C.P., 1993. The paradox of pelagic food webs in the northern Bering Sea-III. Patterns of primary productivity. Continental Shelf Research 13, 575–599.

Stabeno, P.J., Napp, J.M., Mordy, C.W., Whitledge, T.E., 2010. Factors influencing physical structure and lower trophic levels of the eastern Bering Sea shelf in 2005: sea ice, tides and winds. Progress in Oceanography 85, 180–196. http://dx.doi.org/10.1016/j.pocean.2010.02.010.

Stabeno, P., Kachel, N., Moore, S., Napp, J., Sigler, M., Yamaguchi, A., Zerbini, A., 2012. Comparison of warm and cold years on the southeastern Bering Sea shelf. Deep Sea Research Part II. http://dx.doi.org/10.1016/j.dsr2.2012.02.020.

Stigebrandt, A., 1984. The North Pacific: a global-scale estuary. Journal of Physical Oceanography 14, 464–470.

Thompson, R.O.R.Y., 1979. Coherence significance levels. Journal of the Atmospheric Sciences 36, 2020–2021. http://dx.doi.org/10.1175/1520-0469(1979) 036<2020: CSL>2.0.CO;2.

Wadley, M.R., Bigg, G.R., 2002. Impact of flow through the Canadian Archipelago and Bering Strait on the North Atlantic and Arctic circulation: an ocean modelling study. Quarterly Journal Royal Meteorological Society 128, 2187–2203.

Walsh, J.J., McRoy, C.P., Coachman, L.K., Goering, J.J., Nihoul, J.J., Whitledge, T.E., Blackburn, T.H., Parker, P.L., Wirick, C.D., Shuert, P.G., Grebmeier, J.M., Springer, A.M., Tripp, R.D., Hansell, D.A., Djenidi, S., Deleersnijder, E., Henriksen, K., Lund, B.A., Andersen, P., Muller-Karger, F.E., Dean, K., 1989. Carbon and nitrogen cycling within the Bering Chukchi seas: source regions for organic matter effecting AOU demands of the Arctic Ocean. Progress in Oceanography 22 (4), 277–358.

Weingartner, T.J., Cavalieri, D.J., Aagaard, K., Sasaki, Y., 1998. Circulation, dense water formation and outflow on the northeast Chukchi Sea shelf. Journal of Geophysical Research: Oceans 103, 7647–7662.

Weingartner, T.J., Danielson, S., Sasaki, Y., Pavlov, V., Kulakov, M., 1999. The Siberian Coastal Current: a wind and buoyancy-forced arctic coastal current. Journal of Geophysical Research: Oceans 104, 29697–29713.

Weingartner, T.J., Aagaard, K., Woodgate, R.A., Danielson, S., Sasaki, Y., Cavalieri, D., 2005. Circulation on the north central Chukchi Sea shelf. Deep Sea Research Part II. http://dx.doi.org/10.1016/j.dsr2.2005.10.015.

Weingartner, T., E. Dobbins, S. Danielson, P. Winsor, R. Potter, and H. Statscewich, 2013. Hydrographic variability over the northeastern Chukchi Sea shelf in summer-fall 2008–2010. Continental Shelf Research, http://dx.doi.org/10.1016/j.csr.2013.03.012i

Wijffels, S.E., Schmitt, R.W., Bryden, H.L., Stigebrandt, A., 1992. Transport of freshwater by the oceans. Journal of Physical Oceanography 22, 155–162.

Wilkin, J.L., Chapman, D.C., 1987. Scattering of Continental Shelf waves at a discontinuity in shelf width. Journal of Physical Oceanography 17 (6), 713–724.

Wilkin, J.L., 1988. Scattering of Coastal-Trapped Waves by Irregularities in the Coastline and Topography. PhD. Thesis. Woods Hole Oceanographic Institution, Woods Hole, MA, 121p.

Wilson, J.G., Overland, J.E., 1986. Meteorology. In: Hood, D.W., Zimmerman, S.T. (Eds.), The Gulf of Alaska, Physical Environment and Biological Resources, Alaska Office, Ocean Assessments Division, National Oceanic and Atmospheric Administration, U.S. Department of Commerce, 655pp.

Winsor, P., Chapman, D.C., 2004. Pathways of Pacific water across the Chukchi Sea: a numerical model study. Journal of Geophysical Research: Oceans 109 (C3). http://dx.doi.org/10.1029/2003JC001962.

Woodgate, R.A., Aagaard, K., Weingartner, T.J., 2005a. A year in the physical oceanography of the Chukchi Sea: moored measurements from autumn 1990–1991. Deep Sea Research II 52 (24–26), 3116–3149. http://dx.doi.org/10.1016/j.dsr2.2005.10.016.

Woodgate, R.A., Aagaard, K., Weingartner, T.J., 2005b. Monthly temperature salinity, and transport variability of the Bering Strait throughflow. Geophysical Research Letters 32, L04601. http://dx.doi.org/10.1029/2004GL021880.

Woodgate, R.A., Aagaard, K., Weingartner, T.J., 2006. Interannual changes in the Bering Strait fluxes of volume, heat and freshwater between 1991 and 2004. Geophysical Research Letters 33, L15609. http://dx.doi.org/10.1029/2006GL026931.

Woodgate, R.A., Weingartner, T.J., Lindsay, R.W., 2010. The 2007 Bering Strait oceanic heat flux and anomalous Arctic sea–ice retreat. Geophysical Research Letters 37, L01602. http://dx.doi.org/10.1029/2009GL041621.

Woodgate, R.A., Weingartner, T.J., Lindsay, R., 2012. Observed increases in Bering Strait oceanic fluxes from the Pacific to the Arctic from 2001 to 2011 and their impacts on the Arctic Ocean water column. Geophysical Research Letters 39, L24603. http://dx.doi.org/10.1029/2012GL054092.

Zhang, X., Walsh, J.E., Zhang, J., Bhatt, U.S., Ikeda, M., 2004. Climatology and interannual variability of Arctic cyclone activity: 1948–2002. Journal of Climate 17, 2300–2317.

Zhang, Y.-C., Zhang, L.-F., Wang, W.-G., 2010. Interannual sea level variability in the North Pacific Ocean and its mechanisms. Chinese Journal of Geophysics 53 (1), 54–63.